Improving Sentinel-3 SAR Mode Processing Over Lake Using Numerical Simulations

François Boy, Jean-François Crétaux, Malik Boussaroque, and Céline Tison

***Abstract*— Access to fresh water is a key issue for the next decades in the context of global warming. The water level of lakes is a fundamental variable that needs to be monitored for this purpose. The radar altimetry constellation brings a worldwide means to this question. Recent advances in radar altimeter onboard tracking modes have allowed monitoring thousands of lakes and rivers. Now, measurements are widely available with better resolution: it is time to drastically improve the processing. The altimetry waveforms over lakes are difficult to analyze and very different from the ocean ones. We face a large variety of signals due to surface roughness, lake geometry, and environment. The inversion process, named retracking, shall be able to describe all these components. We propose here a retracking based on physical simulations taking as inputs the lake contour and the instrument characteristics. Fitting the simulation on the waveforms gives the water surface height. The algorithm has been tested on the Sentinel-3A and Sentinel-3B time series over Occitan reservoirs (France) and Swiss lakes and compared to *in situ* references. Over small Occitan reservoirs (few ha to few km^2), the unbiased root-mean-square error (ub-RMSE) is better than 14 cm. Over the medium-size Swiss lakes, the ub-RMSE is better than 10 cm for most of them.**

***Index Terms*— Hydrology, lake, radar altimetry, retracking, Sentinel-3, synthetic aperture radar (SAR).**

NOMENCLATURE

C.D.	Cross-track distance to land (km).
DDM	Delay Doppler map.
DEM/DTM	Digital elevation/terrain model.
FFSAR	Fully focused SAR (altimeter).
FSSR	Flat sea surface response.
G-POD	Grid-processing on demand.
IS	Illuminated surface (km).
LPP	Lake processing prototype.
LRM	Low-resolution mode.
mss	Mean square slope (dimensionless).
OCOG	Offset center of gravity.
OLTC	Open-loop tracking command.
PDGS	Payload data ground segment.
PTR	Point target response.
RIP	Range integrated power.
RMSE	Root mean square error.
ub-RMSE	unbiased-RMSE.
SAR	Synthetic aperture radar.
T.L.	Transect length (km).
UFSAR	UnFocused SAR.
WVF	Waveform.
WSH	Water surface height (m).
σ_0	Backscattering coefficient (dB).
Sinc^2	Square sinc function.
$\otimes$	Convolution operator.

Manuscript received July 5, 2021; revised October 6, 2021 and December 9, 2021; accepted December 11, 2021. Date of publication December 20, 2021; date of current version March 8, 2022. *(Corresponding author: François Boy.)*

François Boy and Céline Tison are with the Centre National d'Etudes Spatiales (CNES), 31400 Toulouse, France (e-mail: francois.boy@cnes.fr).

Jean-François Crétaux is with the Centre National d'Etudes Spatiales (CNES), 31400 Toulouse, France, and also with the Laboratoire d'Etudes en Géophysique et Océanographie Spatiale (LEGOS), 31400 Toulouse, France (e-mail: jean-francois.cretaux@cnes.fr).

Malik Boussaroque is with Ocean-Next, 38660 La Terrasse, France, and also with the Laboratoire d'Etudes en Géophysique et Océanographie Spatiale (LEGOS), 31400 Toulouse, France (e-mail: malik.boussaroque@legos.obs-mip.fr).

Digital Object Identifier 10.1109/TGRS.2021.3137034

I. INTRODUCTION

IT WAS pointed out in the Paris Agreement of the United Nations Framework Convention on Climate Change (UNFCCC) the urgent need for perennial observational infrastructures allowing to monitor the climate system and its natural components. Essential climate variables (ECVs) were defined in the Global Climate Observing System (GCOS) Implementation Plan in order to address the question of "closing the Earth's energy balance and the carbon and water cycle" (GCOS 2016). In particular, the lakes serve as "sentinels, regulator, and integrator of the climate change" [1] at regional and global scales and contribute to the Earth water cycle, which describes the continuous movement of water between (semi) permanent storages at, above, and below the Earth's surface [2]–[10]. In such context, the lake storage change is a fundamental variable allowing us to understand the balance between water inputs and water losses, and their linkage with the climate system. This is one of the major indicators allowing understanding the impact of climate change on continental water resources. However, lake storage change is not directly measurable, and it requires generally combining water height and extent variation of lakes that can be observed using remote sensing techniques [11]–[13]. The question of sustainability and global distribution of observations is moreover crucial for continuous and broad monitoring of ECVs, particularly in the case of lakes survey. Lake's water level has, therefore, been defined by GCOs as one of the ECVs, which needs particular attention, in order to detect climate signals at different spatial and temporal scales.

Over land, global data centers store and release long-term *in situ* measurements for the different components of the water

cycle, generally organized in the shape of the global terrestrial network (GTN) in coordination with GCOS. Since 2009, the state hydrological institute (SHI), under the auspice of GCOS, gathers and archives *in situ* data on lake heights with the objective to cover at least the 100–200 largest lakes on the Earth. It is, however, a challenging objective because *in situ* gauges require consequent means from the countries, which they cannot always cope with.

Remote sensing brings a worldwide observation of the Earth, which can address the need for freshwater monitoring, even if it raises questions on temporal and spatial accuracies. Among other sensors, the radar altimeter constellation collects heights over land on a very regular basis. Over the last 30 years, satellite radar altimetry has been a successful technique for monitoring the lake height variations [14], [15]. Current data processing can be fairly simple or complex depending on the mission and the instrument tracking methods. Data acquisition is not affected by weather conditions, but the technique can have a number of limitations and often contain significant errors associated with both technical errors of the measurements themselves and methodological problems of data processing. Rapidly varying topography may inhibit the retrieval of good elevation data. Water level accuracies are also dependent on target size and surface roughness, which will limit worldwide surveying and limnological applications. However, there is the scope for systematic continental-scale monitoring, and the provision of new stage information where gauge data is absent. Anyway, the technique is sufficiently advanced to have enabled a number of inland water case studies. Lake water level time series is gathered in several online databases (DAHITI [16], Hydroweb [17], G-Realm [18], or TEP [19]) with contributions from altimeter observations.

Altimetry has been originally designed to measure sea level height [20], [21], and the first altimeters (TOPEX/Poseidon, Jason-1/Poseidon, and ENVISAT/RA) have been optimized for the ocean. The onboard tracker acquired the signal in its window only in an autonomous manner (closed-loop mode), analyzing how previous acquisitions move inside the window to track the next ones [22]. On continental surfaces, due to strong topography dynamics, the autonomous tracker often fails to detect the water surface echo. Yet, when the altimeter manages to acquire the lake or river signals, the estimation is very valuable, as demonstrated early in the literature [5], [14], [16], [23], [24]. With the initial LRM of altimeters, the accuracy of the estimations is around few centimeters above very large lakes, such as Great Lakes, USA [23], and at decimeter level for smaller lakes [24], [25].

All these promising results encouraged an upgrade of the radar hardware design in the last decade. The OLTC mode [26], [27] has been first tested on Jason-2 and then extended to Jason-3, Sentinel-3, and Sentinel-6. An onboard DEM defines water bodies' location and elevation all along the satellite tracks [28]. The altimeter reads this information in real time to set its reception window over those in-land water targets, also named "virtual stations" (VSs). Recent works have demonstrated the high improvement of successful acquisitions brought by the OLTC mode with a comparison to the historical closed-loop mode [29]. As a consequence, Sentinel-3A (v6.0) and Sentinel-3B (v3.0) OLTCs have been upgraded in 2020. More than 70 000 VSs (rivers or lakes crossings with the satellite tracks) on both Sentinel-3A & B have been defined in the DEM and detected with a success score higher than 85% [27]. Extension above 60° N (previous OLTC versions were limited to this latitude band) is also available, offering the capability to observe lakes in high latitude regions that are exposed to freeze during winter. This high densification comes with the addition of numerous small size (few km^2) to middle size lakes (<50 km^2), observed at nadir or up to 4-km cross-track, so many complex situations for which current data processing are limited. More than the lakes' area, the short distances to the lake edge (<9 km, Sentinel-3A antenna footprint radius) make the radar measurements difficult to exploit. Indeed, the signal is exposed to land contamination. Fortunately, the synthetic aperture radar (SAR) mode [30] implemented on Sentinel-3 and Sentinel-6 greatly improves the azimuth resolution. However, water/land contaminations still occur in the cross-track direction making the signal interpretation still difficult.

The data collection over lakes is now very rich, but new inversion algorithms dedicated to these complex situations need to be developed to fully benefit from the capability of the SAR mode coupled with OLTC. Okeowo *et al.* [31] and Nielsen *et al.* [32] already challenged the existing retracking methods over large lakes (>50 km^2), reaching, respectively, an RMSE between 0.09 and 1.2 m over 30 lakes (Brazil, Nigeria, and the USA) and between 0.19 and 0.3 m over Canada and the USA (excluding icy lakes). In [33], similar performance is reached with Sentinel-3 with an RMSE between 0.03 (large lake) and 1 m.

With the new SAR modes and the capability of observing very small water bodies due to OLTC mode, the retracking algorithms have to be reviewed. The retracking names the inversion process of the altimeter waveforms to the geophysical parameters, among them the WSH. Several algorithms have been developed so far, but very few are dedicated to inland waters observations. For the last 40 years, major retracking developments have been performed for ocean surfaces [34]–[36], conventional LRM altimeters, and, more recently, SAR altimeter [37]–[39]. Ocean retrackers lean on a physical waveform model, which has been built and optimized for open-ocean observations, for conditions where the entire radar footprint contains water. These retrackers are only suitable for the largest inland water bodies. SAMOSA+ [40] is an enhanced version of SAMOSA that includes the mss (closely related to the surface roughness) for processing peaky waveforms (specular surfaces) as the one observed over inland waters and sea ice. The surface roughness is a key parameter over inland waters since it can make the waveform shape evolves from diffuse (broaden when rough) to specular (peaky when smooth). However, the SAMOSA+ model still accounts for an open ocean situation and, thus, cannot model complex lakes geometry. To overcome this limitation, Gao *et al.* [41] have proposed to use SAMOSA+ on limited waveforms range gates, selected using an input DEM, to discard range gates with land contamination. The issue of outliers (mainly due to land contamination) has been discussed in several

publications [16], [42], [43]. However, this work leads to a high mean RMSE of 0.28 m over the Ebro river and 0.16 m over the Ribarroya reservoir.

Empirical approaches have been also proposed with thresholding methods to detect the leading edge of the waveform, among them is the OCOG algorithm [44]. It is the baseline retracker for hydrology in the Sentinel-3 PDGS products. It is very robust, and the output is always available. However, errors are large when the waveform shape evolves (see Section III-C). The method proposed in this article is in the continuation of numerical retracking over the ocean proposed by Boy *et al.* [38] and adapted here to lakes observations. This approach consists of simulating altimeter waveforms and using it as a model inside the retracking algorithm. It gives the advantage to model with high accuracy the altimeter system, accounting for all its characteristics (PTR and antenna diagram) and the scene geometry (satellite orbit, radar delay/Doppler footprint, and lake shape). The altimeter waveforms are simulated using a lake contour to get the most reliable measurement geometry. With the method proposed here, we aim at increasing the survey of the dozens of thousands of lakes and reservoirs that are overpassed by the Sentinel-3A and Sentinel-3B in the SAR mode [45], addressing complex situations.

First, this article presents an analysis of altimeter waveforms' shape variability over lakes (see Section III) and then assesses the corresponding OCOG errors. Some recommendations on the processing are then issued. From all these, an enhanced retracking method for lakes is proposed and illustrated in some study cases in Sections IV and V. A more extensive validation is proposed in Section VI.

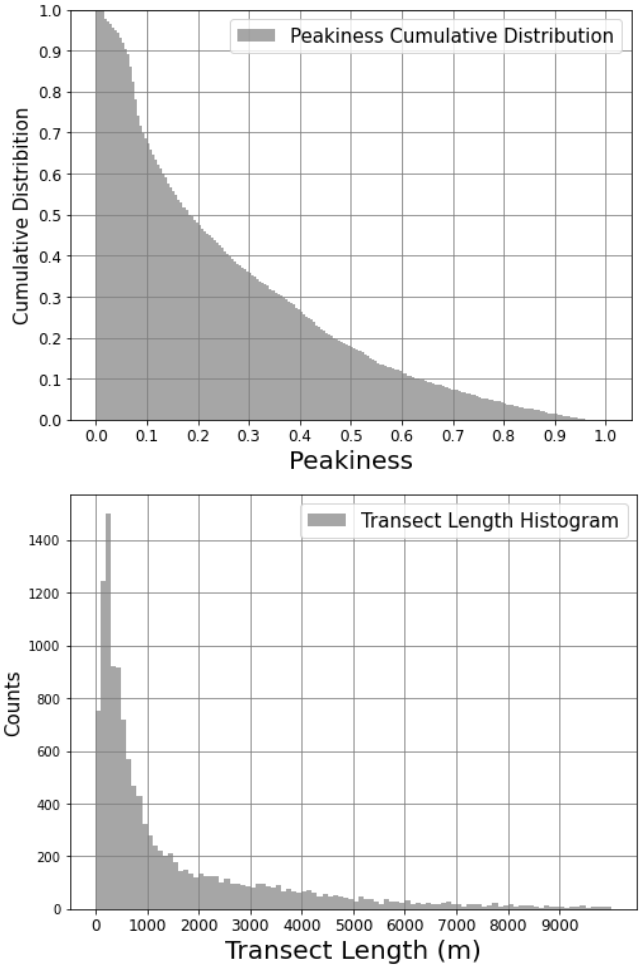

Fig. 1. (Top) WVF peakiness cumulative distribution over lakes (13 000+) defined in the Sentinel-3A OLTC tables and cycle 45 data (June 2019). (Right) Lakes T.L. histogram.

II. Phenomenology of Lake Altimetry Waveforms

A. Illustrations of SAR Waveforms Over Lakes

First, the Sentinel-3 waveforms' morphology has been analyzed over lakes to understand the key parameters required for their description. For all lakes coded inside the Sentinel-3A OLTC version 4, the peakiness has been computed for each waveform located at the center of the water body.

The peakiness criterion is defined as

$$\text{peakiness} = \frac{\max(w_i)}{\sum_{i=1}^{n} w_i} \tag{1}$$

where w is the SAR waveform defined over n gates and w_i is the power of the SAR waveform in gate i.

The peakiness gives an indication of the waveform shape and provides a first understanding of how the signal backscattering behaves. Is it close to a perfect square sinc function or to an ocean-like echo? Lakes' surfaces are smoother than the ocean, with evidently no or at least very much fewer waves. A basic approximation is to consider the lake surface as a mirror, resulting in response close to the radar PTR (Sinc^2). Reality is much more complex.

The peakiness enables to classify the waveforms with respect to their shapes. A peakiness score between 0.5 and 1 corresponds to "sinc^2" class waveforms. Indeed, a sinc^2 function that is exactly centered on a range gate and is sampled at its bandwidth has only one sample at 1 and all others at 0. In that case, peakiness equals 1. If the centering is in the middle of a range gate, the sinc^2 function has two samples at 0.5 and all others at 0. Here, peakiness equals 0.5.

Then, the more the energy is spread in the waveform, the lower the peakiness is. Over the ocean, for example, peakiness is close to 0.05.

The analysis of real Sentinel-3A waveforms over cycle 45 (June 2019) shows a large variety of peakiness, emphasizing that shapes are very different from a lake to another (see Fig. 1).

1) 20% are very peaky (peakiness > 0.5), close to the radar PTR (sinc^2-like).
2) 30% have low peakiness (<0.1). This implies the surface is rough, and waveforms tend to ocean-like shape.
3) 50% have intermediate peakiness with shape in between ocean-like and sinc^2-like.

Mean waveforms (see Fig. 2) for these three peakiness classes illustrate well how shapes evolve with peakiness.

This first observation demonstrates that a simple empirical model cannot cope with this large diversity of situations encountered over lakes. In addition, an ocean retracker cannot

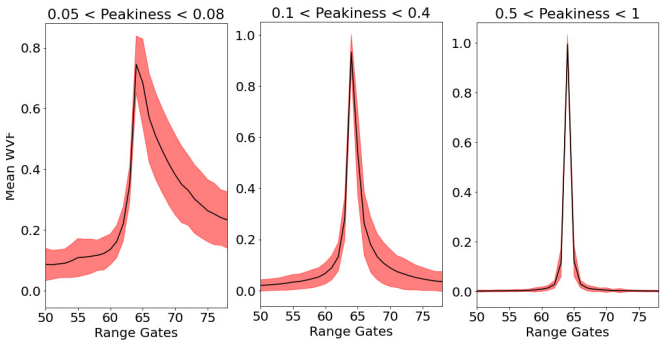

Fig. 2. Mean waveform shapes (black line) and three-sigma deviation (red envelop) for three peakiness classes: (Left) ocean-like, (Middle) intermediate, and (Right) sinc^2.

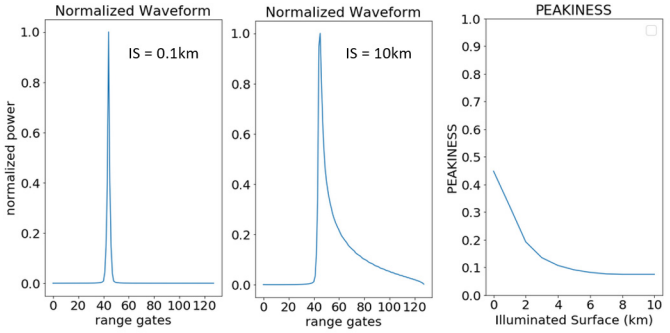

Fig. 3. Normalized simulated SAR waveforms with (Left) IS = 0.1 km, (Center) IS = 10 km, and (Right) peakiness variation as a function of IS.

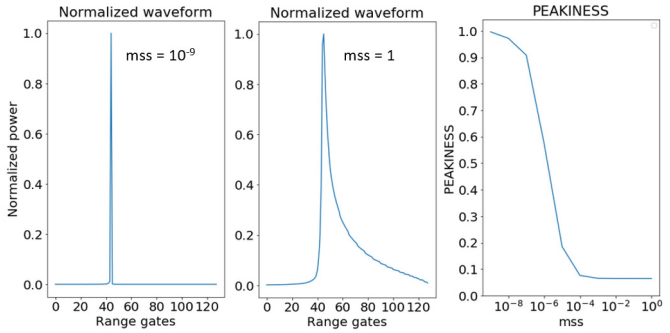

Fig. 4. Normalized simulated SAR waveforms with (Left) mss = 10^{-9}, (Center) mss = 1, and (Right) peakiness variation as a function of mss.

model properly the WVF with high peakiness values. To get accurate and precise WSH, the model used inside the retracking must account for the physics that is responsible for these complex behaviors.

B. Impact of MSS and Illuminated Surface on the Waveform Peakiness

Two main factors lead to change in the waveform shape.

IS: The maximum water surface included in the radar footprint, which is a band strip of ∼320-m along-track and 18-km cross-track in the SAR mode (9 km on either side of the nadir location).

Roughness of the Surface (mss): The mss is the statistical parameter describing the slopes of the surface at all scales (from capillary waves to large waves). For Gaussian height distribution, it is equal to the variance. The mss is approximately linearly related to the wind speed [46], [47].

When the IS is small, few range gates receive signals. Naturally, the resulting waveform will be very peaky. The limit case is when a single scatter is illuminated by the radar, so the resulting waveforms are the point target of the instrument (sinc^2 function). On the opposite, when the surface is large, the entire radar footprint is located over water, and all range gates will receive a signal. The waveform tends to the ocean-like situations. For a given lake, one must keep in mind that the IS can change along the satellite track, depending on the intersection between the lake geometry and the radar footprint.

In addition, surface roughness plays an important role in the waveform shape. Although the IS is large, the signal received in far-range gates may be largely attenuated due to the low roughness of the surface. This happens when no wind stresses the water surface. In such a situation, waveforms are very peaky. The geometrical optics (GOs) also called the Kirchhoff model for the stationary phase correctly model the signal attenuation with respect to the incidence angle of the target [48] and the mss parameter, which characterizes the roughness of the surface

$$\sigma 0(\theta) = \sigma 0(0) e^{-\frac{\sin(\theta)^2}{\text{mss}}} \tag{2}$$

where $\sigma 0$ is the radar signal power (dB) as a function of the incidence angle $\ominus$ and mss is the mean-square slope (dimensionless).

Using simulations (whose principle is described in Section IV [38]), we illustrate how those two key parameters impact the waveform shape. In the following, first (see Fig. 3), we simulate SAR waveforms changing the IS (IS = 4 km means that water is included up to 2 km in the cross-track direction on either side of the nadir location). When IS increases, the peakiness decreases. With the assumption of a rough surface (mss fixed to 1), waveforms are ocean-like over large surfaces and tend to sinc^2 when reducing the IS. However, on small surfaces, the peakiness remains high even if the surface is rather rough.

The second example (see Fig. 4) shows how the waveforms' shape evolves with respect to the surface roughness. When mss increases (from smooth to rough surface), the peakiness decreases. Here, the IS is fixed at 10 km.

An accurate retracking shall lean on waveform modeling, which integrates both information. If not, the WSH time series will be impacted because of the time and/or space variations of the IS and mss. It is well illustrated with the following examples too.

Fig. 5 shows S3A pass 558 normalized waveforms (descending track) over the Gimone lake, which is a small French reservoir observed at nadir on a very small section (∼1 km × 1 km). In November 2016, waveforms are very peaky and sharp. We suppose winds to be low at this date, and as a consequence, the water surface does not present any roughness. In April 2018, waveforms are still peaky since the IS is small but much spread out than in the previous case, certainly due to strong wind stress of the water surface.

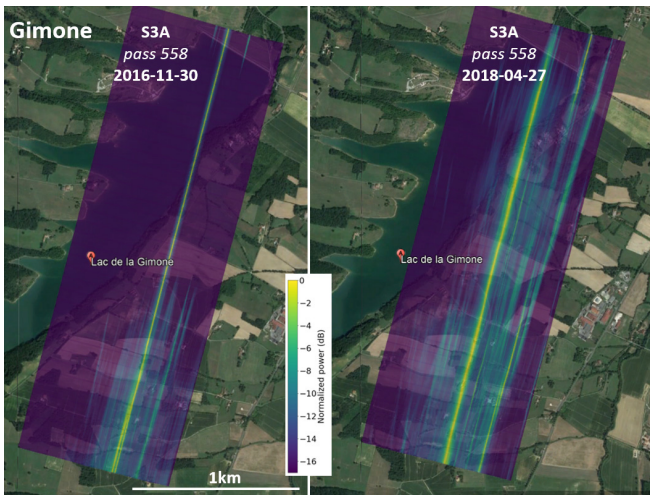

Fig. 5. S3A pass 558 (descending track) normalized waveforms over Gimone lake (France) in two separated dates: (Left) November 30, 2016 and (Right) April 27, 2018. Credits: Google Earth. Waveform starts at the left end.

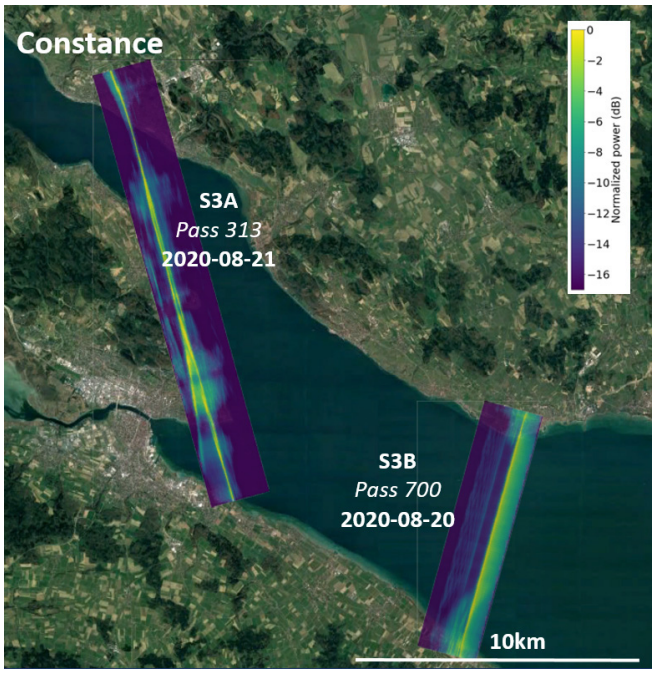

Fig. 6. S3A pass 313 and S3B pass 700 normalized waveforms over Constance lake (Switzerland). Credits: Google Earth.

Fig. 6 shows S3A pass 313 (ascending track) and S3B pass 700 (descending track) normalized waveforms over the Constance lake, the largest lake in Switzerland. Both satellites overfly the lake at different locations. While the S3B track is located in the middle of the lake with large IS, S3A flies over small sections (few kilometers). As a consequence, S3A waveforms are peakier than S3B ones that tend to be close to ocean, such as waveforms. On top of this, the surface roughness will modulate the waveforms' shape, and the ground landscape may add contaminations (S3A-313 example).

C. OCOG Errors

OCOG [44], [49] is the most commonly used retracker for hydrology [32] even if it has acknowledged limits. This is an empirical retracker that computes the leading edge of the waveform from the center of gravity of the power integral. The leading edge is then converted into WSH.

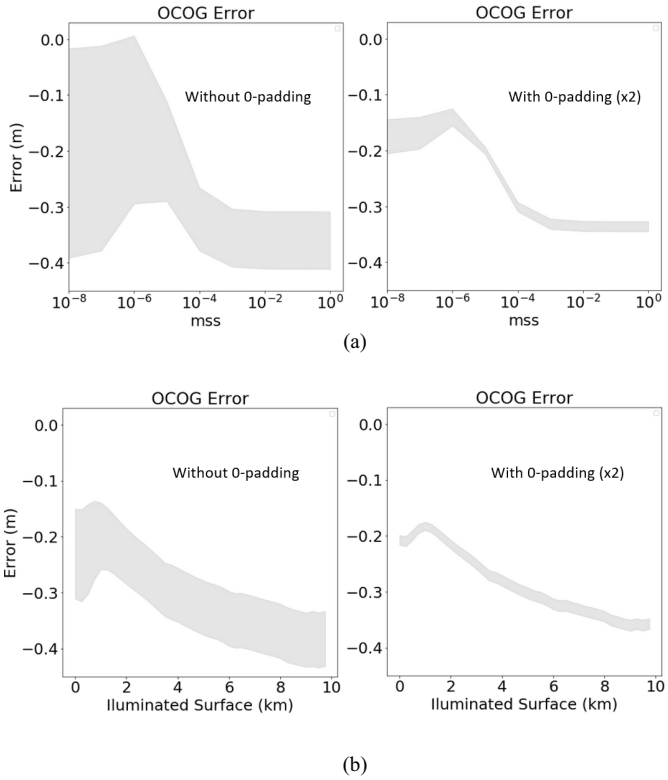

Fig. 7. (a) OCOG error as a function of mss: (Left) without zero-padding and (Right) with zero-padding $\times 2$. (b) OCOG error as a function of IS: (Left) without zero-padding and (Right) with zero-padding $\times 2$.

Knowing how the waveforms change depending on the IS and mss, we assess the OCOG accuracy using the same types of simulations. Fig. 7(a) illustrates the OCOG error, which dramatically changes depending on the mss value (up to 37 cm). This means that the WSH time series will artificially evolve depending on wind conditions.

In addition, different simulations have been run changing the waveform centering inside a given gate (leading edge in gate 44 or 44.5 for example). Again, the OCOG bias changes [gray envelop, Fig. 7(a)], and the corresponding WSH will move depending on where the signal is received inside the range gate.

For very low mss (10^{-8}), this error is about 37 cm too. These errors are similar in the large or small lake cases (not shown).

Fig. 7(b) shows the same assessment but on waveforms that have been zero-padded by a factor 2 (oversampling). The OCOG error variation w.r.t. mss is largely reduced but still important (15 cm). The envelope is almost removed, meaning that there is no more sensitivity to waveform centering.

Similar observations are done when assessing the OCOG errors as a function of the IS. The zero-padding prevents geometrical errors but cannot compensate for roughness variations.

Moreover, as often mentioned in the literature [50], the water backscattering signal can be contaminated with signals

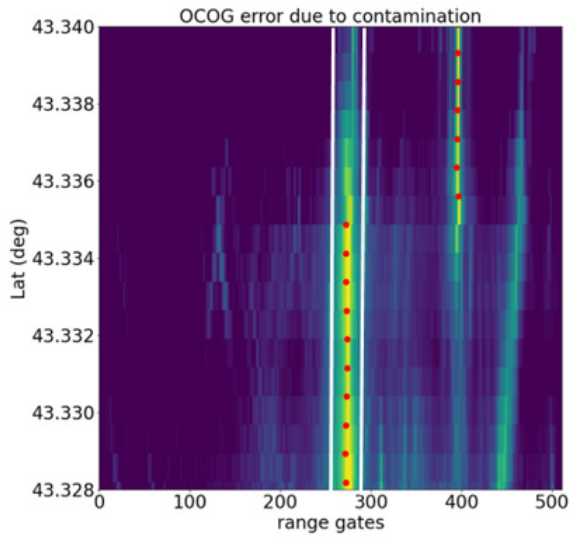

Fig. 8. S3A Normalized waveforms (oversampled by factor 4) over Gimone lake (April 27, 2018). The red dot is OCOG retracking outputs, and white lines indicate where the water signal is located. OCOG is trapped by a more energetic signal coming from surroundings at the top of the plot (latitude around 43.338°).

coming from the surrounding environment. It is obvious that this will occur mostly for small lakes or for mountainous areas. Unfortunately, the OCOG retracker is often trapped by these contaminations, as illustrated in Fig. 8. It is of the highest importance to apply a contamination rejection process prior to any retracking to avoid these situations that lead to metrics errors, whatever the chosen retracking algorithm.

D. Slant Range Errors

In the last OLTC version onboard Sentinel-3A & B, a lot of small lakes (<1 km^2) have been added and even lakes that are not observed at nadir. Considering that the satellite tracks can move by ± 1 km from a cycle to the next one, this implies that some lakes will be observed with a slant range geometry. None of the current retracking approaches accounts for this type of situation. A 500-m on-ground satellite tracks' deviation generates a 15 cm of range error. Again, it appears crucial to include observation geometry in the model used in the retracking.

E. Recommendations for the Processing

Based on the previous observations, it appears mandatory that the processing accounts for the physics and observation geometry in order to address efficiently complex situations. This leads to the following conclusions and recommendations.

A physical retracker is required to consider both the geometry and the roughness of the lake surface. Here, we propose to extend the numerical retracking proposed by [38] over the ocean to lake observations. Section IV details the numerical simulation principle.

In order to avoid the retracking being trapped by contaminations, waveforms must be cleaned up prior to being processed. Processing the waveforms individually, as it is commonly done in altimetry, deprives ourselves to discriminate effectively signals coming from either the water surface or other targets (land, buildings, other water bodies, and so on). Thus, we recommend exploiting the entire radar acquisition over the lake to detect a clear signature in the radargram. Numerical simulations, considering the DEM and the lake shapes, provide the WVF 2-D pattern. It is then possible to detect this pattern in the radargram to discard all the signals that are not related to the water bodies. Section V details the proposed retracking approach.

Level1B processing has to be improved with respect to the standard proposed in the PDGS. First, the spatial sampling shall be increased in order to better observe the small lakes. The FFSAR mode [51] can be a good option for small lakes. However, FFSAR on Sentinel-3 data induces replicas that degrade the signal quality over a water body longer than 100 m. This can also be a major hint when several water bodies are close to each other. The UFSAR mode at 80 Hz is a good compromise, providing an 80-m posting rate with 320-m along-track resolution. We also highly recommend using oversampled waveforms using zero-padding by a factor of 2. The Hamming weighting[1] function is also beneficial over inland waters, reducing the hooking effect brought by the azimuth impulse response. The last two recommendations will be available in the incoming new PDGS version. In the frame of this study, European Space Agency (ESA) Sentinel-3A & B grid-processing on-demand (GPOD) have been used to generate the waveforms (http://gpod.eo.esa.int/services/SARvatore_Services/). The applied configuration is an UFSAR processing at an 80-Hz posting rate with zero padding by a factor of two and the Hamming weighting function.

III. Simulation of SAR Altimetry Waveforms Over Lakes

The simulation of SAR altimeter waveforms over the lake is the core process of the proposed approach. For each satellite pass over the lake, numerical simulations of the radar waveforms are built using a lake contour. All satellite and instrument characteristics are accounted for radar antenna diagram, radar PTR, tracker information, satellite track position, altitude, and *a priori* WSH. This last one corresponds to the value included in the onboard OLTC table. The methodology is inherited from [38], where we have proposed numerical simulations to process Cryosat-2 SAR mode data over the ocean. This approach has been only updated to account for the lake geometry. The notations and the geometry are described in Fig. 9.

For each GPOD 80-Hz UFSAR measurement (M) available in the product, the radar delay/Doppler footprint is computed and projected over the lake contour. As a Hamming weighting function is applied during the UFSAR processing, the footprint is a $\sim$450-m wideband strip in the along-track direction. In the across-track direction, the radar delay/Doppler footprint is limited by the pulse-limited radius (9 km). The intersection between the band strip and the lake contour gives the water surface that is illuminated and observed by the radar (blue

[1]Hamming weighting is a raised cosine function to minimize the Gibbs effect.

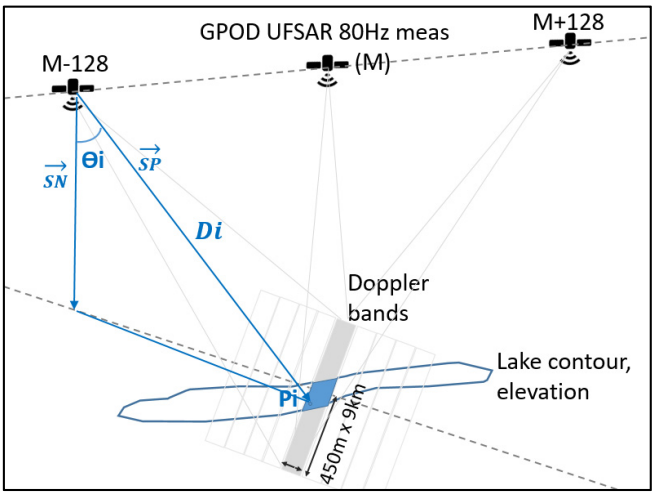

Fig. 9. Simulation scheme. M is the considered measurement. For M, the signals acquired in the 128 previous and 128 following measurements are taken into account and combined in the SAR processor.

area). The IS is digitalized with 5 m × 5 m pixels (pixels are named P_i latter, i being the pixel index). At this stage, all pixels are considered at the same elevation given by the onboard OLTC.

The waveform available in the GPOD product is the result of a multilooking process. The simulation must reproduce this principle. All measurements that contributed to the waveform computation are identified (128 measurements before/after M). However, to speed up the process, only one over four is accounted for as it is done for most SAR models over the ocean. Hereafter, those measurements are called "looks" or l in formulas. The simulation loops over the looks and generates a corresponding flat surface response (FSR) together with the local incidence angles matrix (θ).

For each look, the process loops over all pixels. For each pixel P_i, the distance between the satellite and the pixel (D_i) is computed. The satellite position is extracted from the GPOD product (latitude, longitude, and altitude) and converted into Cartesian coordinates. The pixel coordinates are known using the lake contour, and its elevation is taken from the prior WSH given by the OLTC. D_i is simply computed as a Euclidean distance between the satellite and the pixel. Then, the range R_i is computed removing the onboard tracker window delay from D_i. The window delay is extracted from the GPOD product. R_i is then converted in range gates (speed light c over two times the radar bandwidth B), accounting for the zero-padding (pad, oversampling rate of 2), to determine in which gate r_i, the signal, will fall inside the radar window

$$R_i = (D_i \text{WindowDelay}) \times \frac{\frac{c}{2\times B}}{\text{pad}} \tag{3}$$

where pad is the oversampling factor. At the same time, the incidence angle θ_i defined as the angle between $\underset{\text{SP}}{\longrightarrow}$ (satellite to pixel vector) and $\underset{\text{SN}}{\longrightarrow}$ (satellite to nadir vector) vectors is computed and recorded. The nadir on-ground Cartesian coordinates are computed from satellite coordinates. The received gain G_i is computed accounted only for the antenna

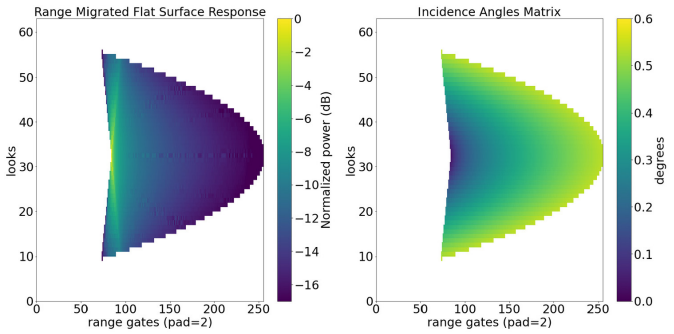

Fig. 10. Example of (Left) simulated FSRrmc and (Right) incidence angles matrix computed over lake Leman for a given measurement in the middle of the lake.

gain and θ_i as the following:

$$\theta_i = \arccos \frac{\underset{\text{SN}}{\longrightarrow} \cdot \underset{\text{SP}}{\longrightarrow}}{\left\| \underset{\text{SN}}{\longrightarrow} \right\| \left\| \underset{\text{SP}}{\longrightarrow} \right\|}$$

$$G_i = \exp\left(-8\log(2)\left(\frac{\theta_i}{\theta_{3\text{ dB}}}\right)^2\right) \tag{4}$$

where $\theta_{3\text{ dB}}$ is the antenna 3-dB aperture (1.34°).

For all pixels, the corresponding G_i is sorted and accumulated by range gate r_i. This is resulting in the FSR, $FSR(l, r)$, and the incidence angles, $\theta(l, r)$. As described in [38], range migration is then applied on FSR as it is done during the UFSAR processing in order to align all looks in range. This gives FSR_{rmc} matrix. The incidence angles matrix is migrated in accordance (see Fig. 10).

FSR_{rmc} is then multiplied by a function that describes how signal power decreases as a function of the incidence angles matrix [GO model; see (2)]. FSRrmc is then summed over looks to get the multilooked FSR [$\text{ML}_{\text{FSR}}(r)$]

$$\text{ML}_{\text{FSR}}(r, \text{WSH}, \text{mss}) = \sum_{l=-128}^{l=128} \text{FSR}_{\text{rmc}}(l, r, \text{WSH}) e^{-\frac{\sin(\theta(l,r)^2}{\text{mss}}}. \tag{5}$$

Then, the convolution with the instrument PTR is applied in the Fourier domain. The following simulated waveform is obtained for each measurement acquired over the lake:

$$\text{wvf}_s(r, \text{WSH}, \text{mss}) = P_u * \text{IFFT}[\text{FFT}(\text{ML}_{\text{FSR}}(r, \text{WSH}, \text{mss}))) \times \text{FFT}(\text{PTR}(r))] \tag{6}$$

with

$$\text{PTR}(r) = \left| \frac{\sin\left(\pi \frac{r}{\text{res}}\right)}{\pi \frac{r}{\text{res}}} \right|^2 \tag{7}$$

where

wvf_s	simulated waveform;
P_u	radar power;
r	in radar range dimension;
FSR_{RMC}	range migrated FSR;
$\ominus$	incidence angle;
WSH	water surface height;
mss	mean square slope;
PTR	point target response.

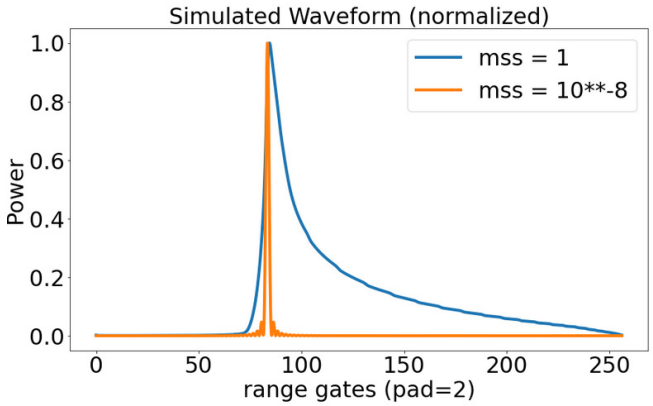

Fig. 11. Example of simulated waveforms over lake Leman for a given measurement in the middle of the lake. Waveforms are plotted for mss = 0 (rough surface) and mss = 10^{-8} (smooth surface).

Note that simulations are done with a very high zero-padding factor (64) for accurate computation. Then, simulated waveforms are undersampled to fit the zero padding applied on the GPOD product (oversampling of a rate equal to 2).

The three adjustment input parameters of the model are WSH, mss, and Pu. The FSR, which depends only on WSH, is computed once at an *a priori* initial WSH. This prior is the height from the onboard OLTC. Then, to test for other WSH values, the FSR is simply shifted by 1/64 gate (8 mm).

The PTR should be defined as a 2-D function, in range and looks (azimuth direction). The azimuthal component is not accounted for here for simplifying the computation. This has impacted at centimeter level.

Intentionally, the significant wave height is not accounted for in the model in order to reduce the dimensions of the model. Over small to middle size lakes, it appears that this choice has no impact on the overall performances.

The soil contribution is supposed to equal to 0.

The L1B configuration used to process Sentinel-3 data is accounted for (factor-2 zero-padding, the Hamming weighting function, and 80-Hz posting rate; see results section).

Fig. 11. shows how simulated waveform over lake Leman evolves when mss varies from 1 to 10^{-8} to model rough or smooth water surface. The waveform varies from a sinc^2 function to an open ocean-like shape just because of the mss.

Figs. 12 and 13 illustrate the quality of the numerical simulations. Both examples show that the simulation can cope with large to small lakes. In the lake Leman simulation, the lake edge signature is well reproduced. In the Gimone case, the surface water is cross-track observed at 43.31° latitude. As a consequence, waveforms are sliding in the window (slant range effect) what is accurately reproduced in the simulation since the acquisition geometry is intrinsically accounted for.

IV. Three Steps Retracking Based on Numerical Simulations

With the altimeter waveforms simulation at the heart of the process, we propose three steps retracking over lakes.

A. Global Retracking

The first retracking step is global, meaning the inversion is applied to the entire radar acquisition sequence along the lake.

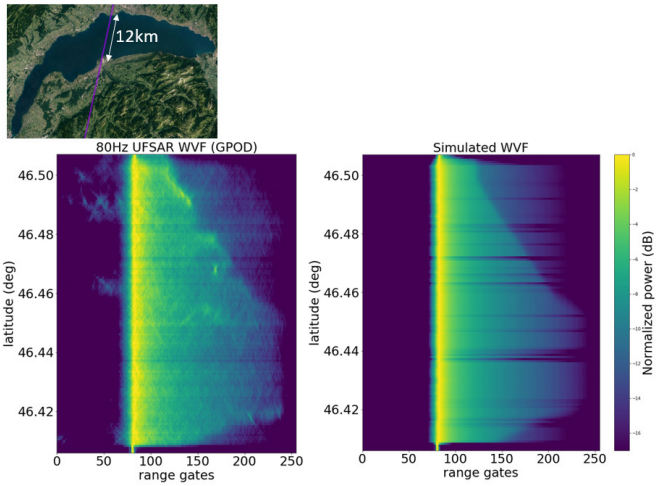

Fig. 12. S3A real normalized waveforms over (Left) lake Leman (January 16, 2017), Switzerland, and (Right) corresponding final simulated waveforms. Waveforms are normalized and plotted in dB. Simulation is the one obtained at the end of the retracking (see Section III).

This first step aims at locating roughly the water signal inside the radargram in order to reject contaminations, rather than estimating accurate WSH and mss. The objective here is to find the couple (WSF, mss) which provide the closest simulated radargram to the measured one. So, the global retracking leans on a least-squares method, minimizing the sum of the squares of the residuals between the radargram and the full numerical simulation (model). Due to chaotic shapes of hydrological WF, the convergence was hardly reached, leading us to simply compute the least square criterion for all possible couples (WSH, mss). P_u (radar power), as being a simple scaling factor of the model, does not impact the minimization result. It can be estimated separately. Eventually, the couple minimizing the criterion is taken. To reduce the number of possible values, WSH is tested from gates 0 to 127 with 1/8th gate step, and $\log_{10}$(mss) is tested from −8 to 0 dB with 1-dB step. Again, the goal here is to approximately locate the water signal inside the radargram. This first global retracking provides a single evaluation of WSH1st and mss1st for the entire radar acquisition along the lake.

B. Contamination Rejection

The contamination rejection consists of editing all signals that are not included in the numerical simulations computed during the global retracking. All the signals that are not resulting from the lake water surface are removed to avoid the final retracking step to be trapped by spurious signals.

To reach this selection, all the range gates with a simulated normalized power below −20 dB are rejected. In addition, a maximum of ten gates around the gate of WSH1st are kept.

C. Individual Retracking

Now, the waveforms have been cleaned up; individual waveforms' retracking can be safely performed. "Individual" means here that the retracking is applied in 1-D for each measurement. The simulation is again run to estimate the precise

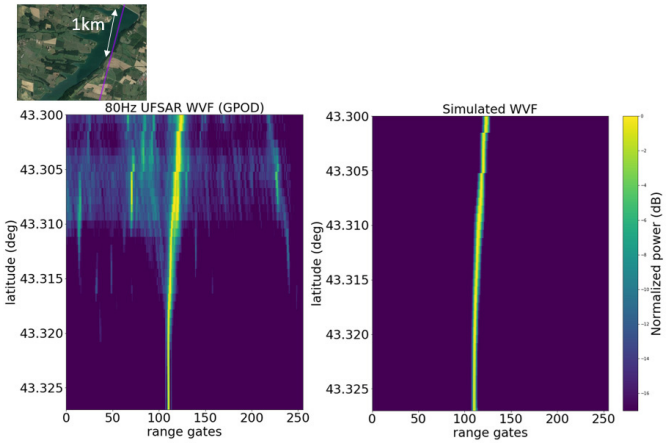

Fig. 13. S3A Real normalized waveforms over (Left) Gimone reservoir (April 25, 2020), France, and (Right) corresponding final simulated waveforms. Waveforms are normalized and plotted in dB. Simulation is the one obtained at the end of the retracking (see Section III).

WSH parameter. For each measurement, the corresponding numerical simulation is used through a least-squares estimator to estimate WSH and mss parameters. Here, we intend to get the final estimates with better accuracy. WSH is tested ± 1 gate around WSH_1st with 1/64 step, and $\log_{10}$(mss) is tested from -8 to 0 dB with a 0.25-dB step.

D. Water Surface Height Corrections and Editing

Finally, the WSH is obtained by applying geophysical and atmospherical corrections

$$\mathrm{WSH}_{\mathrm{corr}} = \mathrm{WSH} - \mathrm{GEO}_{\mathrm{corr}} - \mathrm{ATM}_{\mathrm{corr}} \quad (8)$$

$$\mathrm{ATM}_{\mathrm{corr}} = \mathrm{WTC} + \mathrm{DTC} + \mathrm{IC}. \quad (9)$$

WTC is the wet tropospheric correction, DTC is the dry tropospheric correction, and IC is the ionospheric correction. These three corrections are released in GPOD products and are based on models over continental water bodies. GEOcorr includes the tidal corrections (terrestrial and polar) and the geoid correction (EIGEN6C4). As for the atmospheric corrections, they are all released in the GPOD products.

For small lakes, the errors of the geoid undulations at short wavelengths are negligible and, from one cycle to another one, are averaged. For the largest lakes, it would be necessary to correct for geoid undulation using the repeat track technic as detailed in [15].

To build the final WSH, measurements acquired at nadir over the lake are selected. If no nadir measurement is found, off-track acquisitions up to 1 km are selected. Selected WSH estimates are edited using two criteria:

WSH shall not deviate from the global retracking by more than $\pm$ a half gate.

The mean quadratic error between the simulated waveform and the waveforms (both normalized) shall not be higher than 0.04. This value has been set up empirically.

To finish, edited WSH are averaged using a three-sigma iterative outliers' rejection rule [56] in order to get only one value per lake and per track. The principle is the following one. The mean value and standard deviation of individual WSHs are computed. All WSH values outside ± 3 times the standard deviation around the mean value are rejected. Then, mean and standard deviation are computed again without accounting for outliers detected during the previous step. Values outside the new computed boundaries are rejected and so on until no outliers are detected. The averaged WSH (single value per track) is the mean value of WSHs without all outliers detected during the iterative process. Last but not least, all the processing is fully automatic. There is no manual editing.

E. Step-by-Step Illustration

Fig. 14 illustrates, step by step, the processing of GPOD 80Hz UFSAR waveforms [see Fig. 14(b)] over lake Gimone [see Fig. 14(a)]. First, the global retracking fits the simulation over the entire radar acquisition sequence along the lake [see Fig. 14(c)]. The rejection contamination process is applied, and waveforms are cleaned up [see Fig. 14(d)]. Finally, for each measurement, the individual retracking fits the simulation over the decontaminated waveform. A WSH is estimated for each measurement and compared to PDGS OCOG outputs and *in situ* references [see Fig. 14(e)]. When the radar overflights the lake at nadir (around lat $= 43.335°$), the estimates are very accurate, whereas OCOG shows a bias of 30 cm. Then, when the satellite flies away from the lake, OCOG estimates quickly fall down by almost 1 m, impacted by the slant range effect. Our technique, accounting for the acquisition geometry, provides stable estimates although accuracy is slightly degraded. In parallel, mean-square slopes are estimated [see Fig. 14(f)]. The values vary between 2.10^{-6} and 1.10^{-7} in this example.

F. CPU and Memory Usage

LPP has been optimized in terms of CPU and memory usage; 500-MB memory and 30 s of CPU time are required per km. It remains some margin of improvement to get fully operational processing for ground segments, which was out of the scope of our work.

V. Validation

In the following, our technique will be called LPP.

LPP has been applied on two sets of lakes in two different regions: Occitanie (South of France) and Switzerland. Whole S3A and S3B missions have been processed from the beginning up to July 2020 (which corresponds to 52 passes for S3A and 21 passes for S3B).

Lake contours are extracted from the CARTHAGE database [53] for French lakes and from the SWOT Lake database [52] for Swiss lakes.

Daily *in situ* measurements have been provided by the Electricité De France (EDF) for Occitan lakes and the Office Fédéral de l'Environnement (OFEV, Switzerland, https://www.hydrodaten.admin.ch/) for Swiss Lakes. Both sets of *in situ* references have been converted into EIGEN6C4 for a direct comparison with LPP WSH estimates.

The sizes of the lakes vary from hundreds of meters in width for the smallest to few kilometers for the biggest. The surrounding topography is very different from one site to

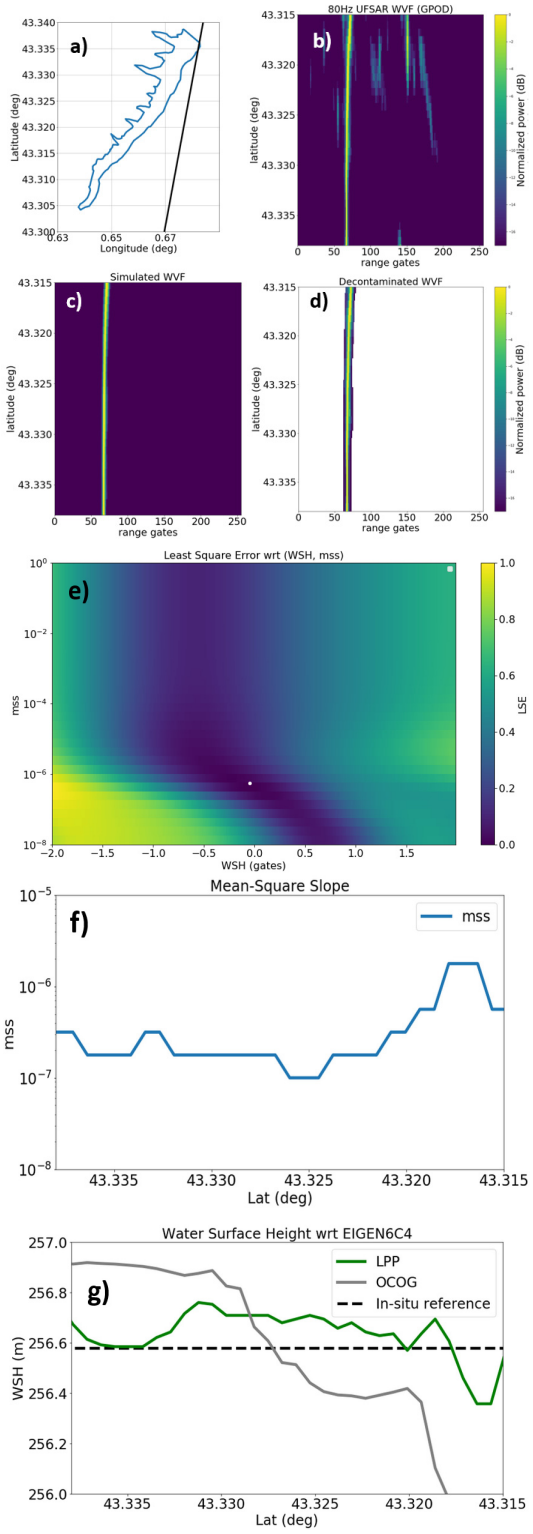

Fig. 14. Data processing, step by step over Gimone lake, S3A descending pass 558. (a) Lake contour with satellite track. (b) GPOD 80Hz UFSAR normalized waveforms. (c) Simulated waveforms as the output of the global retracking. (d) GPOD 80-Hz UFSAR normalized waveforms after contamination rejection process. (e) 2-D plot of least-squares error in mss-WSH space for measurement at lat = 43.315°, and white point is the (mss and WSH) estimated couple that minimizes the LSE criterion over the lake Gimone. (f) WSH estimation from our technique (green), from PDGS OCOG (gray), and from *in situ* measurements (dashed black line). (g) Estimated mean-square slope.

another: some are in mountainous areas, whereas others are in open areas.

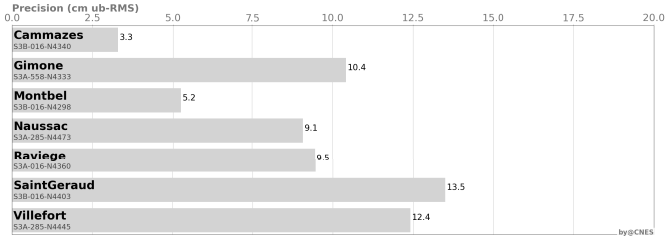

Fig. 15. LPP performances over Occitan lakes (ub-RMSE in cm).

TABLE I

LIST OF OCCITAN LAKES IN FRANCE. VS: VIRTUAL STATION NAME INDICATING THE LAKE LOCATION OVER THE SATELLITE PASS (NORTH AND LATITUDE IN 0.01°); *M*: MISSION S3A OR S3B; *P*: SATELLITE PASS; *A*: AREA; T.L.: SATELLITE TRANSECT LENGTH OVER LAKE; C.D.: CROSS-TRACK DISTANCE TO LAND (AT MAXIMUM); AND WSH: WATER SURFACE HEIGHT (FROM OLTC TABLES)

Lake	VS	M	P	A km²	T.L. km	C.D. km	WSH m
Gimone	N4333	S3A	558	2.8	1.2	0.5	267
Naussac	N4473	S3A	285	10.8	2.6	1.2	953
Raviege	N4360	S3A	16	4.4	0.5	0.7	665
Villefort	N4445	S3A	285	7.3	0.25	0.6	597
Cammazes	N4340	S3B	16	7.7	0.3	0.7	579
Montbel	N4398	S3B	16	17.3	2	1.5	399
St-Geraud	N4403	S3B	16	5.7	0.1	0.3	375

A comparison with HYDROWEB is performed in Section VI-C in order to identify in which conditions LPP improves WSH estimates.

Only WSHs are validated using *in situ* measurements. The mss estimates are not validated and discussed in this article. Work is ongoing to cross-compare mss with wind measurements, which will be part of a future publication as it requires further analysis.

A. Occitan Lakes

Table I details Occitan lakes' characteristics. All are small size reservoirs with the area (A) below 10 km^2, excepted Montbel which has a 17.3 km^2 area. Satellite T.L. over the lakes is very short, from 100 m for Saint-Géraud to a maximum of 2.6 km for Naussac. The maximum C.D. is 1.2 km for Gimone and 1.5 km for Montbel; elsewhere, C.D. is well below 1 km. Considering that the Sentinel-3 tracks move by ±1 km from one cycle to the following, this means that all lakes with C.D. below 1 km are sometimes not observed at nadir. All those characteristics indicate that radar observations will be highly contaminated by land and with complex geometry. WSH estimation is very challenging for all of them.

LPP performances are presented hereafter (see Fig. 15). ub-RMSE is below 14 cm for all lakes with even only 3.3 cm for Cammazes. For this lake, off-nadir radar observations are frequent since the track is located at the exact lake shoreline. The LPP strategy gives very high satisfaction over this set of lakes despite the strong complexity of radar observations.

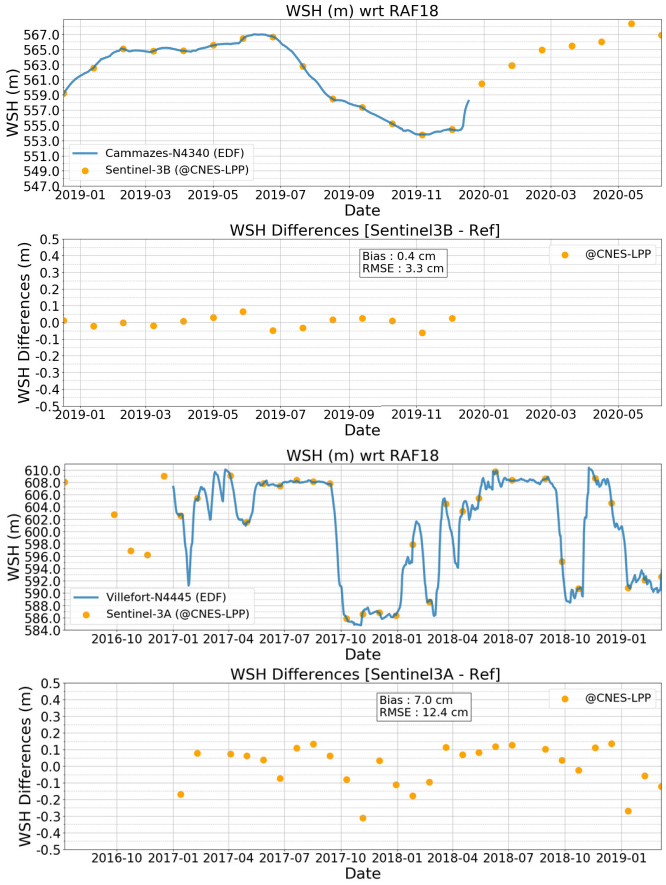

Fig. 16. (Top) LPP (orange dots) and *in situ* reference (blue line) WSH time series over Cammazes and Villefort and differences in (Bottom).

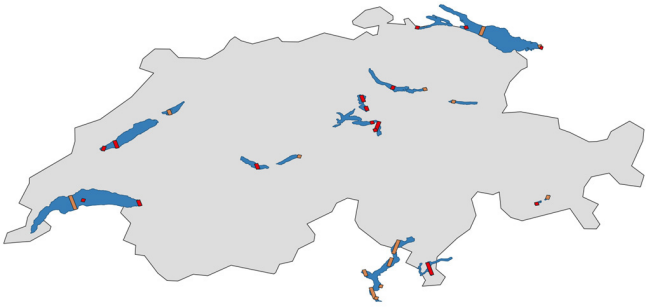

Fig. 17. Map of Switzerland and lakes that are studied here. Polygons are S3A (red) and S3B (orange) VSs.

Ub-RMSE is defined as

$$\text{ubRMSE}^2 = \text{Var}(\text{WSH}_{\text{LPP}} - \text{WSH}_{\text{insitu}} - E(\text{WSH}_{\text{LPP}} - \text{WSH}_{\text{insitu}})). \quad (10)$$

Ub-RMSE enables to qualify only the noise on the estimation and not the bias.

WSHLPP and WSHinsitu are the WSHs measured, respectively, with LPP and provided by *in situ* gauges.

Fig. 16 shows the time series for Cammazes and Villefort. LPP WSH is plotted in orange and *in situ* measurements in blue.

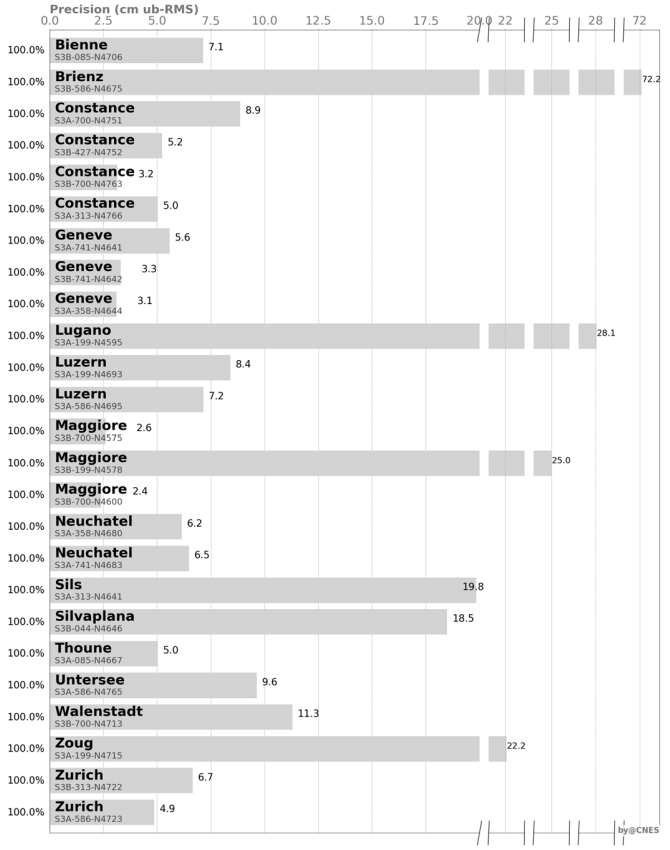

Fig. 18. LPP performances over Swiss lakes (ub-RMSE in cm).

B. Switzerland Lakes

Sentinel-3A and Sentinel-3B data have been processed using the LPP over 17 lakes in Switzerland for 24 VSs in total. The characteristics of each VS are given in Table II, and Fig. 17 provides a map of the region.

They are small (Silvaplana and Sils), middle size (Thoune, Zoug, Walenstadt, and so on), and large lakes (Geneva, Constance, and Maggiore) in mountainous areas. This set offers a high variety of situations. Some overflights do not represent any difficulty, with long transect and C.D., for example, Geneva-N4644, Constance-N4752, Neufchatel-N4683, or Lugano-N4595. Others have shorter transect and/or satellite overflight close to land, for example, Luzern-N4698, Zurich-N4722, or Brienz-N4675. Here, the complexity of the scene is due either to the surrounding relief or to the relative position of the tracks with respect to the lakeshore. Two lakes are located at high altitudes and will be exposed to frost during the winter period. Finally, we also included Constance-N4751, which is not located over the lake but 80 m east overland.

1) Global Results for the 17 Lakes: Fig. 18 presents the LPP performances over this set of lakes. Ub-RMSEs are more contrasted than over Occitan lakes; 18 over the 25 VSs provide a very good ub-RMSE, below 10 cm. It remains seven VSs with relatively low performances, from 11.3 to 72.2 cm.

Those performances have been analyzed using a box plot [see Fig. 19(a); the box-plot description is available in Fig. 19(b)]. It shows that some outliers are responsible for

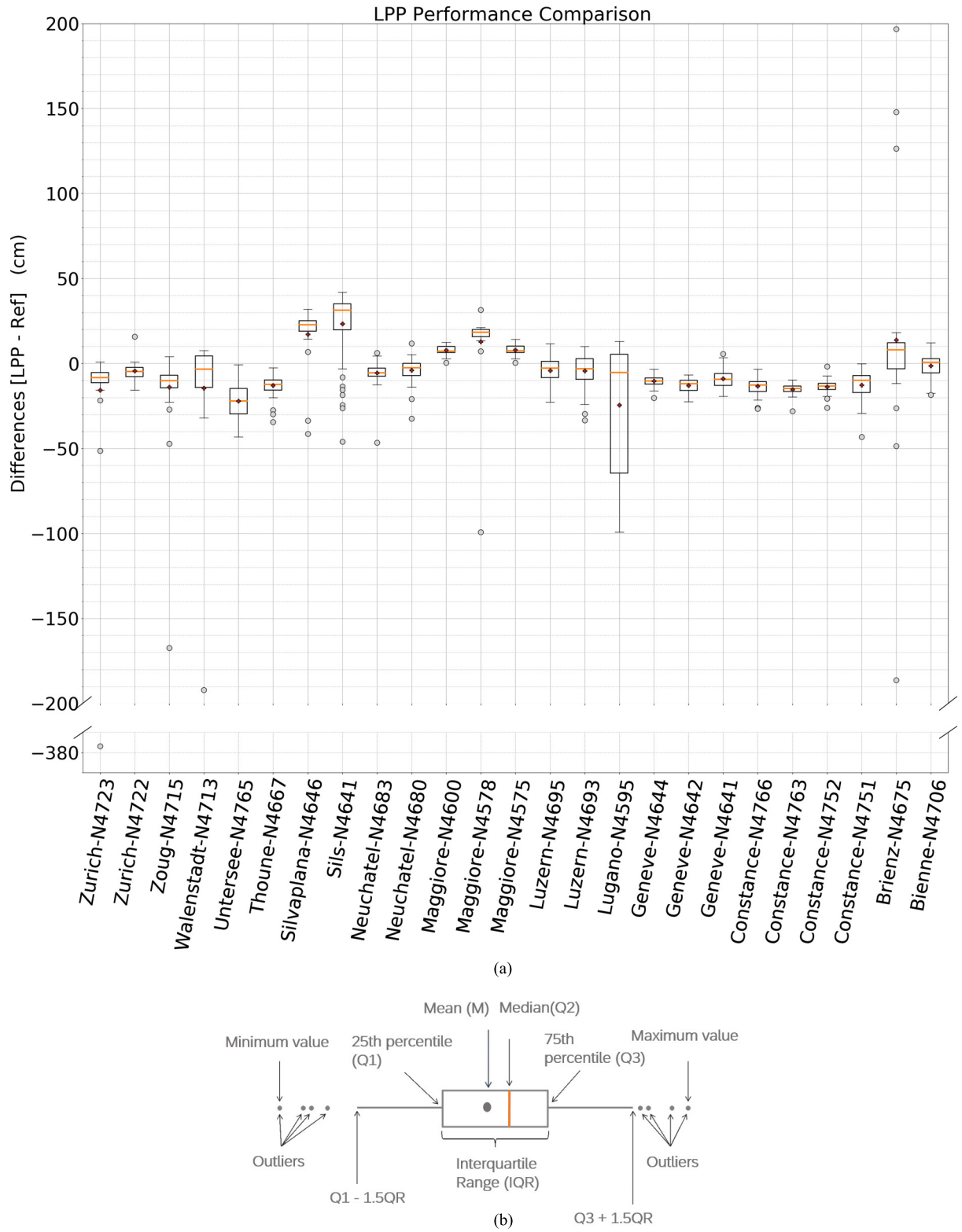

Fig. 19. (a) LPP performances with box plot over Swiss lakes. (b) Box plot description.

higher ub-RMSE for some lakes. It means that the signal is perturbed only at a few dates. All the other acquisitions have very good quality and, thus, accurate estimations. For example, on Magguire-N4578, the size of the box is very narrow, about 5 cm, telling that the majority of passes has a very low WSH error with respect to *in situ* measurements, but one single pass has an error close to approximately −1 m, which degrades then the overall ub-RMSE statistic. The same observation can be done for all lakes with higher ub-RMSE (Wallenstatd-N4713, Zoug-N4715, and so on) except for Lugano-N4595.

2) Investigation of Strong Error Cases and Editing: Radar acquisitions with strong LPP WSH errors have been investigated. Some cases are mainly related to failed acquisitions in closed loop (at the beginning of the missions) or wrong OLTC

TABLE II

LIST OF LAKES IN SWITZERLAND. VS: VIRTUAL STATION NAME INDICATING THE LAKE LOCATION OVER THE SATELLITE PASS (NORTH AND LATITUDE IN 0.01°); *M*: MISSION S3A OR S3B; *P*: SATELLITE PASS; *A*: AREA; T.L.: SATELLITE TRANSECT LENGTH OVER LAKE; C.D.: CROSS-TRACK DISTANCE TO LAND (AT MAXIMUM); AND WSH: WATER SURFACE HEIGHT (FROM OLTC TABLES)

Lake	VS	M	P	A km²	T. D. km	C. D. km	WSH m
Constance	N4751	S3A	700	473	0	0	390
Constance	N4766	S3A	313	473	14.5	8,8	390
Constance (untersee)	N4765	S3A	586	63	0.25	2,8	390
Geneva	N4641	S3A	741	234	4.7	11	370
Geneva	N4644	S3A	358	234	12	30	372
Lugano	N4595	S3A	199	48.7	10	8	272
Luzern	N4695	S3A	586	113	7.3	3,5	431
Luzern	N4698	S3A	199	113	1.3	6,5	431
Neuchatel	N4680	S3A	358	218	3.8	3,3	422
Neuchatel	N4683	S3A	741	218	6.4	17	422
Sils	N4641	S3A	313	4	0.8	1,5	1789
Thoune	N4667	S3A	85	48.3	4.4	5	558
Zoug	N4715	S3A	199	38.3	5.2	2,5	411
Zurich	N4723	S3A	586	88.7	3	11	402
Bienne	N4706	S3B	85	39.3	4	8	425
Brienz	N4675	S3B	586	39.8	1.4	3,7	563
Constance	N4763	S3B	700	473	2.3	6	395
Constance	N4752	S3B	427	473	7.5	26	395
Geneva	N4642	S3B	741	234	11.3	28	371
Maggiore	N4578	S3B	199	215	15	5	193
Maggiore	N4611	S3B	700	215	22	4	193
Silvaplana	N4646	S3B	44	2.7	3	0,8	1789
Walenstadt	N4713	S3B	700	24.2	1.3	9	418
Zurich	N4722	S3B	313	88.7	1.3	6	402

commanding (Lugano-N4595). In other remaining cases, the altimeter is tracking correctly the water surface. However, waveforms are largely degraded, as illustrated in Fig. 20 over lake Lugano. It has not been explained why waveforms deviate so far from the theory. Further work will consist of linking those degraded acquisitions to extreme meteorological events (wind and rain) or to define if land and water signals are melted and cannot be separated by the processing (single large peak containing both water and land).

Anyway, those WSH errors are not linked to LPP failure (the processing is working nominally) but to the quality of the signal. The editing step detects and removes most of the wrong individual WSH estimates, either with the MQE thresholding or with the iterative three-sigma rejection process. However, a few remaining measurements pass all criteria and provide a bad averaged WSH estimate. As a consequence, we have decided to add the last editing step that removes the averaged WSH estimates (entire pass) if more than 80% of individual measurements have been rejected previously.

Fig. 21 presents the LPP performances using the additional final editing step. The ratio of valid passes for each VS is written on the left-hand side of the bar charts.

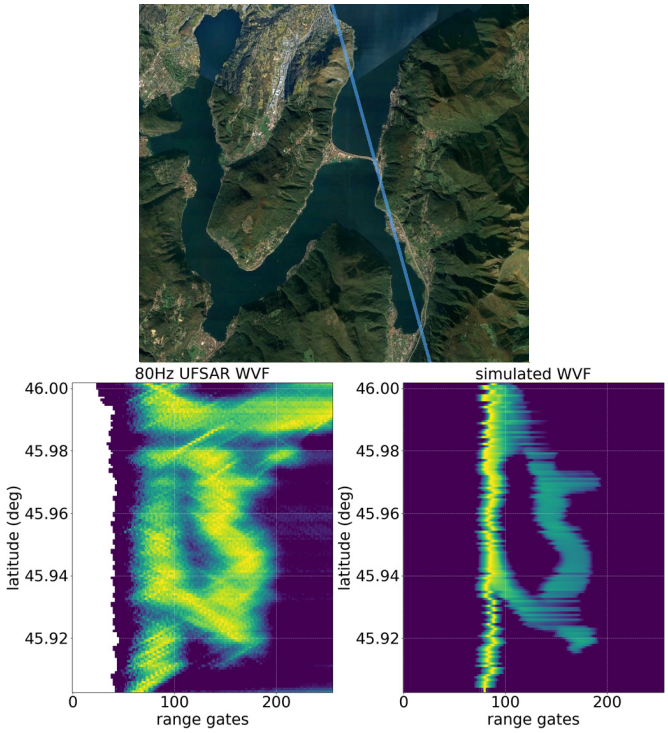

Fig. 20. Landscape with (Left) S3A 199 ascending pass, (Center) GPOD normalized waveforms over lake Lugano, September 9, 2019, and (Right) LPP simulated waveforms.

The ratio is above 95% for all VS (excepted for Lugano-N4595, ∼75%, and Constance-N4751, ∼89%), demonstrating again that, on average, only about one pass every two years provides degraded acquisitions that cannot be processed accurately, which is largely acceptable.

Now, 20 VSs (80%) have a ub-RMSE lower than 7.5 cm. Three cases show lower performances.

Sils-N4641 and Silvaplana-N4646 WSH time series are presented in Fig. 22. Again, some measurements deviate more from *in situ* references, especially during the winter period. Waveforms carry double-peak signals (see Fig. 23), which characterizes frozen surfaces [54]. In such a case, LPP retracks in the middle of the two peaks. As a consequence, the WSH is underestimated compared to *in situ* measurement.

Brienz-N4675 time series are illustrated in Fig. 24. Three passes with a high error are still not rejected despite editing steps. Corresponding waveforms are clearly degraded without any explanation today (see Fig. 25). Further work is needed in order to understand this type of acquisition.

3) Multipass Coverage: Lake Constance Case: Lake Constance provides very good performances and presents an interesting opportunity to go more into detail about the orbital configuration with respect to the lake shoreline. Fig. 26 shows the projection of the Sentinel-3A and Sentinel-3B tracks over lake Constance. S3B-700 offers optimal conditions with a ∼7-km along-track transect in the middle of the lake without cross-track land contaminations. S3A-313 and S3B-427 present much more challenging situations with either land/water alternation short transect (2 km) closed to the lake edge. S3A-700 is even more complicated since the track does not pass over the lake but 80 m east overland.

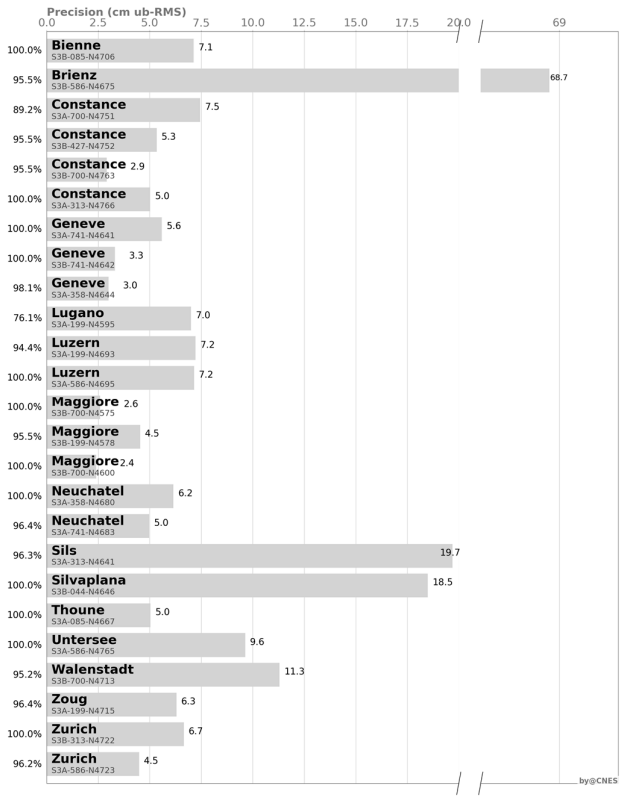

Fig. 21. LPP performances over Swiss lakes (ub-RMSE in cm) applying final editing strategy.

TABLE III
LPP PERFORMANCES OVER LAKE CONSTANCE

M ission/Pass/VS	Bias (cm)	Ub-RMSE (cm)
S3A/313/N4766	-9.6	5
S3B/700/N4763	-13.5	2.9
S3B/427/N4752	-12.1	5.3
S3A/700/N4751	-12.4	7.5

LPP performances are reminded in Table III.

Very similar biases are observed, the maximum deviation between them being only 2.8 cm. The ub-RMSEs are excellent too, with similar numbers whatever is the overflight configuration. It is obvious that S3B-700 provides the best performances (ub-RMSE = 2.9 cm) as the conditions are optimal. However, the ub-RMSEs are very close on S3A-313 (5 cm) and S3B-427 (5.3 cm), whereas land/water contaminations are strong for those tracks. Last but not least, S3A-700 often measures the lake off-track, and the performances remain very good with ub-RMSE equal to 7.5 cm. This is the strength of the proposed approach to offer robust and reliable estimates in complex situations.

Since geoid errors are very small over such lakes, it is then easy to combine several tracks using LPP WSH without the need for intertrack alignment. Fig. 27 shows the LPP WSH time series over lake Constance using the four SVs.

C. Comparison to Hydroweb

The Hydroweb database (http://hydroweb.theia-land.fr) gathers WSH time series over rivers and lakes. The calculation

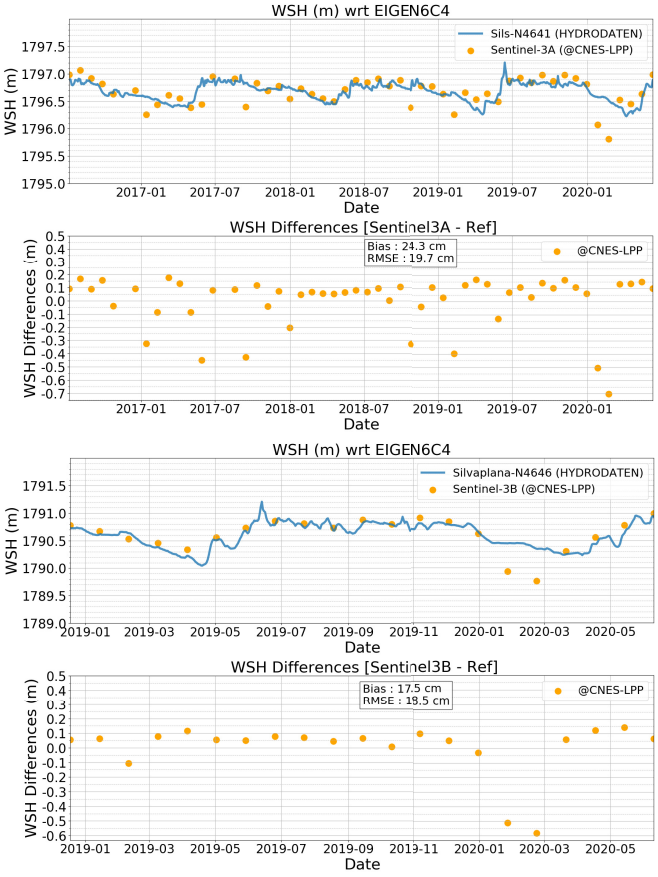

Fig. 22. (Top) LPP (orange dots) and *in situ* reference (blue line) WSH time series over Sils and Silvaplana and differences in (Bottom).

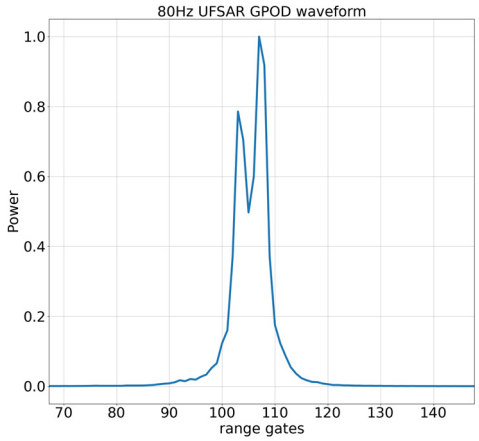

Fig. 23. GPOD waveforms (normalized) with the double-peak during the winter period.

is done using the OCOG retracking measurement, with editing on the backscatter coefficient and the geographical location of the measurements. In contrast to the LPP data processing, if the nadir point measurement is out of the lake contour, the lake is excluded. The editing is, thus, more severe leading to fewer observations. Some additional outliers are also removed using a filter, which considers historical water level variations in an iterative process. Details on the full calculation are given in [15]. In this section, we compare the WSH using the LPP method to the WSH from Hydroweb using a range from

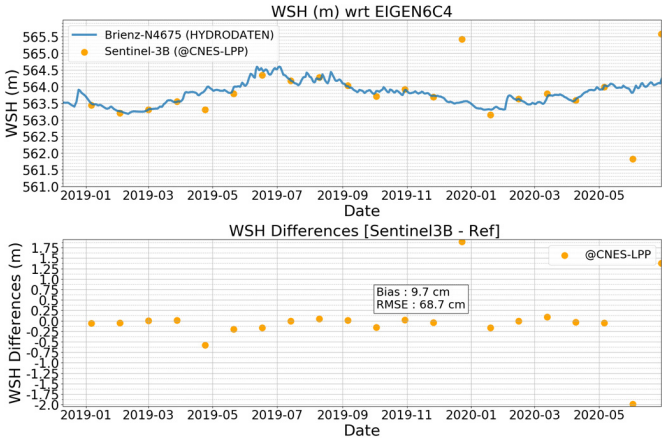

Fig. 24. (Top) LPP (orange dots) and *in situ* reference (blue line) WSH time series over Brienz and differences in (Bottom).

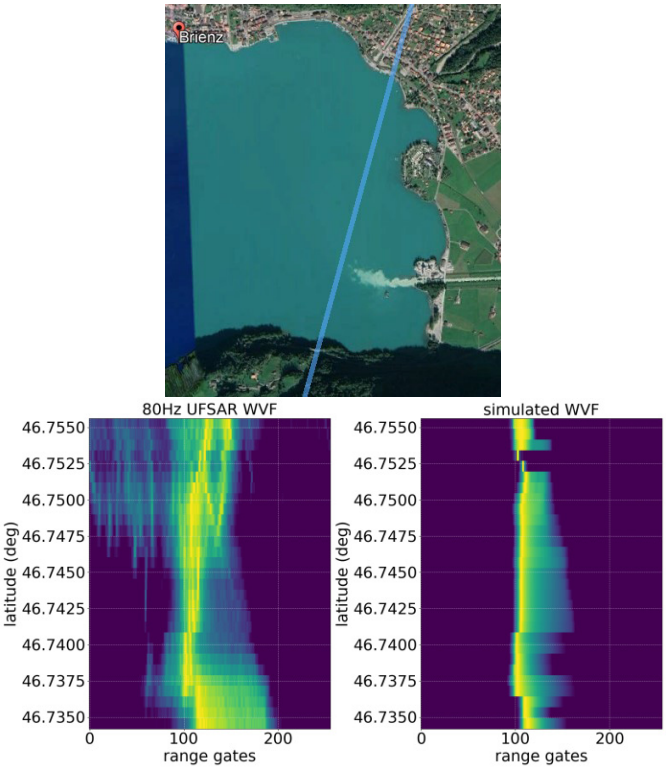

Fig. 25. Landscape with (Left) S3B 586 descending pass, (Center) 80-Hz UFSAR GPOD waveforms over lake Brienz, December 23, 2019, and (Right) LPP simulated waveforms.

OCOG retracker, which is released in the PDGS. For the Swiss lakes, we simply have extracted the WSH of the lakes from Hydroweb. The Occitan lakes are not included in Hydroweb: we have recalculated the WSH using the OCOG retracker and the same data processing as in Hydroweb. As shown previously, the sizes of the lakes vary from hundreds of meters of width for the smallest to few kilometers for the largest. The surrounding topography is very different from one site to another: some are in mountainous areas, whereas others are in open areas. This influences drastically the quality of the data processing with the approach used in Hydroweb. Moreover, for the lake, we have drawn special attention to tracks that

Fig. 26. Lake Constance and corresponding S3A & S3B passes.

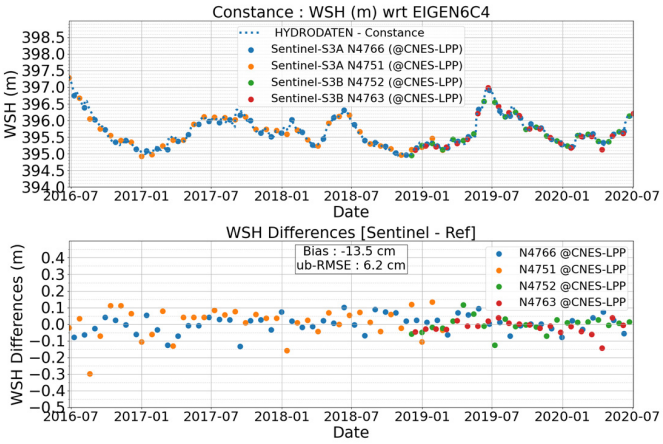

Fig. 27. Multimission LPP times series over lake Constance and comparison to *in situ* measurements.

are in the close vicinity to the lakeshore. For the narrower lakes in the Swiss Alps and Occitanie, the OCOG retracker fails to retrieve a WSH. However, for all others, an accurate WSH has been retrieved in Hydroweb. The estimated height time series were then compared to *in situ* data, as done with LPP, and it highlights that the performances with OCOG remain quite acceptable with accuracy at the decimeter level for the narrowest at the centimeter level for the biggest lake Geneva. For these lakes, LPP and Hydroweb give similar performances, while, for narrow lakes or tracks very close to the shoreline (as over lake Constance with S3A track 313; see Fig. 26), the performances are at least twice better for LPP than for Hydroweb. All the results are summarized in Fig. 28.

Indeed, lake Constance (S3A-313 N4766) presents a complex overflight. The LPP data processing is not at all degraded, with the accuracy remaining at the level 5 cm. For the processing using OCOG/Hydroweb, the WSH accuracy is significantly degraded to around 20 cm. This clearly shows that the LPP data processing is very robust whatever the geometrical configuration since OCOG remains accurate only in favorable conditions. For the majority of large lakes, OCOG can be used with high accuracy, as demonstrated in many

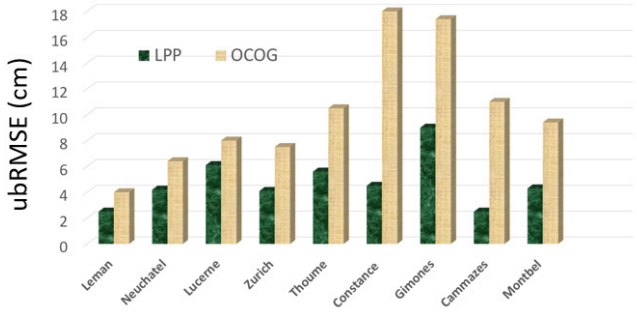

Fig. 28. ub-RMSE of the comparison between altimetry data processing (LPP and OCOG/Hydroweb).

publications, while, for more complicated cases, the LPP is significantly better. This may allow increasing considerably the potential of the Sentinel-3 (*A* and *B*) missions to survey an increase number of small lakes worldwide than what is currently done, in particular within the global database, such as Hydroweb, GRML, or Dahiti.

The comparison between *in situ*, LPP, and OCOG results over the reservoir in Occitanie further accentuates those obtained in Switzerland (see Fig. 28). Over the Gimone lake, even for such a narrow lake, the LPP method allows measuring WSH at few centimeters of accuracy, while, using OCOG, the results remain quite acceptable with accuracy at the decimeter level but two times worse than with the LPP.

For the lakes Cammazes and Montbel, the LPP method is also very accurate with ub-RMSE of few centimeters and still quite accurate with OCOG. For the lake St Geraud, which has a very narrow width of less than 200 m, the LPP method still gives results of around 14 cm of accuracy, while OCOG did not allow calculating the WSH accurately.

VI. Conclusion

Satellite altimetry has become over the years an ideal technique to measure water levels on land, especially over lakes that are counted by millions. With the Sentinel-3A and Sentinel-3B missions, we could potentially monitor thousands of lakes of all sizes through the OLTC mode updates. However, the technique, even in SAR mode, is complex to exploit, and important considerations are to be accounted for to get accurate WSH estimates. The retracking methods, originally designed for the oceans, have to be adapted to describe mixed water/land scenes with low roughness. The variability of the altimetry waveforms is very high, as shown in this article. Two major parameters are the water body shape and its roughness. Empirical retrackers are not able to model properly these both parameters.

In this study, we have developed a new method that considers a number of parameters, such as the geometry of the acquisition and the surface roughness in order to greatly improve the quality of the model used inside the retracking. Although the validation of the mss estimates needs to be addressed in future work to eventually correlate them to local wind variations, it appears essential to include the surface roughness in the radar altimeter echo modeling to improve significantly Sentinel-3 SARM performances over lakes. In addition, this work emphasizes the importance to reject contaminations from radar altimeter echoes before applying any retracking algorithm to avoid large errors.

Due to this new technique based on physical simulation of the waveforms, we can now measure water levels on surfaces for which it was impossible with the retracking algorithms that are commonly used. WSHs measured with the S3A and S3B satellites have been validated on several lakes in Switzerland and in the southwest of France in comparison with *in situ* gauges. Over small Occitan reservoirs (few km^2), the ub-RMSE is better than 14 cm. Over the medium-size Swiss lakes, the ub-RMSE is better than 10 cm for most of them.

These performances often surpass by a factor of at least 2 those of the OCOG retracking. It also even allows measuring water levels where it was unreachable before. This method is automated and will be implemented in the Hydroweb database. This also proves that radar altimeters, even on very small lakes of few ha, allow reaching accuracy as good as laser altimetry (ICESAT2), which has been evaluated in [55].

The demonstration has been made with Sentinel-3 SAR data. The authors plan to extend this work to the Sentinel-6 mission and also to the LRM acquisitions.

Specific work has to be conducted on the echoes for which the LPP fails. The waveforms are really perturbed and distorted. The roughness evolution due to natural events (wind) is very local and rapid. Comparisons with SAR images tend to prove a very high heterogeneity of the lake surfaces. The LPP should take this better into account, at least with more elaborate editing. It has also been observed that, when the surface is frozen, LPP performances are impacted since the echo modeling does account for the double-peak shape of the waveforms. Additional effort is required to cover those situations.

Acknowledgment

The authors thank Claire Pottier [Centre National d'Etudes Spatiales (CNES)] for her support on the lake database and Sophie Le Gac (CNES) for her support on the OLTC database. They also thank the Electricité De France (EDF), France, CTOH (LEGOS), France, and the Office Fédéral de l'Environnement (OFEV), Switzerland, for providing *in situ* data and ESA/European Space Research Institute (ESRIN) for the GPOD processing facility. This work was performed in the frame of collaboration with European Space Reasearch and Technology (ESTEC).

References

[1] C. E. Williamson, J. E. Saros, W. F. Vincent, and J. P. Smol, "Lakes and reservoirs as sentinels, integrators, and regulators of climate change," *Limnology Oceanogr.*, vol. 54, no. 6part2, pp. 2273–2282, Nov. 2009.

[2] I. M. Mason, M. A. J. Guzkowska, C. G. Rapley, and F. A. Street-Perrott, "The response of lake levels and areas to climatic change," *Climatic Change*, vol. 27, no. 2, pp. 161–197, Jun. 1994, doi: 10.1007/BF01093590.

[3] C. Birkett, "Synergistic remote sensing of lake Chad variability of basin inundation," *Remote Sens. Environ.*, vol. 72, no. 2, pp. 218–236, May 2000.

[4] C. Birkett, "The contribution of TOPEX/POSEIDON to the global monitoring of climatically sensitive lakes," *J. Geophys. Res. Oceans*, vol. 100, pp. 25179–25204, Jan. 1995.

[5] J.-F. Crataux *et al.*, "Water balance of the Big Aral Sea from satellite remote sensing and *in situ* observations," *J. Great Lakes Res.*, vol. 31, no. 4, pp. 530–534, 2005.

[6] T. Oki and S. Kanae, "Global hydrological cycles and world water resources," *Science*, vol. 313, no. 5790, pp. 1068–1072, Aug. 2006, doi: 10.1126/science.1128845.

[7] J. Wang *et al.*, "Recent global decline in endorheic basin water storages," *Nature Geosci.*, vol. 11, no. 12, pp. 926–932, Dec. 2018.

[8] S. Biancamaria, F. Hossain, and D. Lettenmaier, "Forecasting transboundary river water elevations from space," *Geophys. Res. Lett.*, vol. 38, pp. 1–5, Jan. 2011.

[9] F. Hossain *et al.*, "Proof of concept of an altimeter-based river forecasting system for transboundary flow inside Bangladesh," *IEEE J. Sel. Topics Appl. Earth Observ. Remote Sens.*, vol. 7, no. 2, pp. 587–601, Feb. 2014.

[10] F. Yao, J. Wang, K. Yang, C. Wang, B. A. Walter, and J.-F. Crétaux, "Lake storage variation on the endorheic Tibetan plateau and its attribution to climate change since the new millennium," *Environ. Res. Lett.*, vol. 13, no. 6, Jun. 2018, Art. no. 064011, doi: 10.1088/1748-9326/aab5d3.

[11] H. Gao, C. Birkett, and D. P. Lettenmaier, "Global monitoring of large reservoir storage from satellite remote sensing," *Water Resour. Res.*, vol. 48, no. 9, Sep. 2012, Art. no. W09504, doi: 10.1029/2012WR012063.

[12] J.-F. Cretaux *et al.*, "Lake volume monitoring from space," *Surv. Geophys.*, vol. 37, pp. 269–305, Oct. 2016, doi 10.1007/s10712-016-9362-6.

[13] T. Busker *et al.*, "A global lake and reservoir volume analysis using a surface water dataset and satellite altimetry," *Hydrol. Earth System Sci.*, vol. 23, pp. 669–690, Feb. 2019.

[14] C. M. Birkett and I. M. Mason, "A new global lakes database for a remote sensing program studying climatically sensitive large lakes," *J. Great Lakes Res.*, vol. 21, no. 3, pp. 307–318, Jan. 1995.

[15] J.-F. Crétaux and C. Birkett, "Lake studies from satellite radar altimetry," *Comp. Rendus Geosci.*, vol. 338, nos. 14–15, pp. 1098–1112, Nov. 2006.

[16] C. Schwatke, D. Dettmering, W. Bosch, and F. Seitz, "DAHITI-An innovative approach for estimating water level time series over inland waters using multi-mission satellite altimetry," *Hydrol. Earth Syst. Sci.*, vol. 19, pp. 4345–4364, Jan. 2015.

[17] J.-F. Crétaux *et al.*, "SOLS: A lake database to monitor in the Near Real Time water level and storage variations from remote sensing data," *Adv. Space Res.*, vol. 47, pp. 1497–1507, May 2011.

[18] C. Birkett, C. Reynolds, B. Beckley, and B. Doorn, "From research to operations: The USDA global reservoir and lake monitor," in *Coastal Altimetry*. Berlin, Germany: Springer, 2011, pp. 19–50.

[19] D. Gustafsson, J. Andersson, F. Brito, B. Martinez, and B. Arheimer, "New tool to share data and models in hydrological forecasting, based on the ESA TEP," in *Proc. EGU Symp.*, Vienna, Austria, Apr. 2018, pp. 8–13.

[20] J. T. McGoogan, "Satellite altimetry applications," *IEEE Trans. Microw. Theory Techn.*, vol. MTT-23, no. 12, pp. 970–978, Dec. 1975.

[21] D. Chelton, J. Ries, B. Haines, L. Fu, and P. Callahan, *Satellite Altimetry, in Satellite Altimetry and Earth Sciences*, L. L. Fu and A. Cazenave, Eds. New York, NY, USA: Academic, 2001, pp. 1–131.

[22] Y. Le Roy, M. Deschaux-Beaume, C. Mavrocordatos, M. Aguirre, and F. Heliere, "SRAL SAR radar altimeter for sentinel-3 mission," in *Proc. IEEE Int. Geosci. Remote Sens. Symp.*, Jul. 2007, pp. 219–222.

[23] C. S. Morris and S. K. Gill, "Evaluation of the TOPEX/POSEIDON altimeter system over the Great Lakes," *J. Geophys. Res.*, vol. 99, pp. 24527–24539, Dec. 1994.

[24] M. Riáko, C. M. Birkett, J. A. Carton, and J.-F. Crétaux, "Intercomparison and validation of continental water level products derived from satellite radar altimetry," *J. Appl. Remote Sens.*, vol. 6, no. 1, Dec. 2012, Art. no. 061710, doi: 10.1117/1.JRS.6.061710.

[25] A. Arsen, J.-F. Crétaux, M. Berge-Nguyen, and R. del Rio, "Remote sensing-derived bathymetry of lake Poopó," *Remote Sens.*, vol. 6, no. 1, pp. 407–420, Dec. 2013.

[26] J. D. Desjonquères, G. Carayon, N. Steunou, and J. Lambin, "Poseidon-3 radar altimeter: New modes and in-flight performances," *Mar. Geodesy*, vol. 33, no. sup1, pp. 53–79, Aug. 2010.

[27] S. Le Gac, F. Boy, D. Blumstein, L. Lasson, and N. Picot, "Benefits of the open-loop tracking command (OLTC): Extending conventional nadir altimetry to inland waters monitoring," *Adv. Space Res.*, vol. 68, no. 2, pp. 843–852, Jul. 2021.

[28] D. Blumstein *et al.*, "Major upgrade of OLTC on Sentinel-3A and 3B in 2018: Benefits for inland waters users," in *Proc. ESA Living Planet Symp.*, Milan, Italy, 2019.

[29] N. Taburet *et al.*, "S3MPC: Improvement on inland water tracking and water level monitoring from the OLTC onboard Sentinel-3 altimeters," *Remote Sens.*, vol. 12, no. 18, p. 3055, Sep. 2020, doi: 10.3390/rs12183055.

[30] R. K. Raney, "The delay/Doppler radar altimeter," *IEEE Trans. Geosci. Remote Sens.*, vol. 36, no. 5, pp. 1578–1588, Sep. 1998.

[31] M. A. Okeowo, H. Lee, F. Hossain, and A. Getirana, "Automated generation of lakes and reservoirs water elevation changes from satellite radar altimetry," *IEEE J. Sel. Topics Appl. Earth Observ. Remote Sens.*, vol. 10, no. 8, pp. 3465–3481, Aug. 2017.

[32] K. Nielsen, O. B. Andersen, and H. Ranndal, "Validation of Sentinel-3A based lake level over U.S. and Canada," *Remote Sens.*, vol. 12, no. 17, p. 2835, Sep. 2020.

[33] G. D. Quartly *et al.*, "The roles of the S3MPC: Monitoring, validation and evolution of Sentinel-3 altimetry observations," *Remote Sens.*, vol. 12, no. 11, p. 1763, May 2020.

[34] G. Brown, "The average impulse response of a rough surface and its applications," *IEEE Trans. Antennas Propag.*, vol. AP-25, no. 1, pp. 67–74, Jan. 1977.

[35] G. Hayne, "Radar altimeter mean return waveforms from near-normal incidence ocean surface scattering," *IEEE Trans. Antennas Propag.*, vol. AP-28, no. 5, pp. 687–692, Sep. 1980.

[36] C. Tourain *et al.*, "Benefits of the adaptive algorithm for retracking altimeter nadir echoes: Results from simulations and CFOSAT/SWIM observations," *IEEE Trans. Geosci. Remote Sens.*, vol. 59, no. 12, pp. 9927–9940, Dec. 2021, doi: 10.1109/TGRS.2021.3064236.

[37] C. Ray *et al.*, "SAR altimeter backscattered waveform model," *IEEE Trans. Geosci. Remote Sens.*, vol. 53, no. 2, pp. 911–919, Feb. 2015.

[38] F. Boy, J.-D. Desjonquères, N. Picot, T. Moreau, and M. Raynal, "CryoSat-2 SAR-mode over oceans: Processing methods, global assessment, and benefits," *IEEE Trans. Geosci. Remote Sens.*, vol. 55, no. 1, pp. 148–158, Jan. 2017, doi: 10.1109/TGRS.2016.2601958.

[39] C. Buchhaupt, L. Fenoglio-Marc, S. Dinardo, R. Scharroo, and M. Becker, "A fast convolution based waveform model for conventional and unfocused SAR altimetry," *Adv. Space Res.*, vol. 62, no. 6, pp. 1445–1463, Sep. 2018.

[40] S. Dinardo, M. Restano, and J. Benveniste, "SAR altimetry processing on demand service for CryoSat-2 and Sentinel-3 at ESA G-POD," in *Proc. Conf. Big Data Space*, Santa Cruz de Tenerife, Spain, Mar. 2016, pp. 15–17.

[41] Q. Gao *et al.*, "Analysis of Retrackers' performances and water level retrieval over the ebro river basin using Sentinel-3," *Remote Sens.*, vol. 11, no. 6, p. 718, Mar. 2019.

[42] C. M. Birkett and B. Beckley, "Investigating the performance of the jason-2/OSTM radar altimeter over lakes and reservoirs," *Mar. Geodesy*, vol. 33, no. sup1, pp. 204–238, Aug. 2010.

[43] K. Nielsen, L. Stenseng, O. B. Andersen, H. Villadsen, and P. Knudsen, "Validation of CryoSat-2 SAR mode based lake levels," *Remote Sens. Environ.*, vol. 171, pp. 162–170, Dec. 2015.

[44] D. Wingham, C. Rapley, and H. Griffiths, "New techniques in satellite altimeter tracking systems," in *Proc. of IGARSS*, vol. 86, Sep. 1986, pp. 1339–1344.

[45] C. Donlon *et al.*, "The global monitoring for environment and security (GMES) Sentinel-3 mission," *Remote Sens. Environ.*, vol. 120, pp. 37–57, May 2012.

[46] C. Cox and W. Munk, "Measurement of the roughness of the sea surface from photographs of the sun's glitter," *J. Opt. Soc. Amer.*, vol. 44, no. 11, pp. 838–850, Nov. 1954.

[47] M. H. Freilich and B. A. Vanhoff, "The relationship between winds, surface roughness, and radar backscatter at low incidence angles from TRMM precipitation radar measurements," *J. Atmos. Ocean. Technol.*, vol. 20, no. 4, pp. 549–562, 2003.

[48] F. Ulaby and D. Long, *Microwave and Radiometric Remote Sensing*. Norwood, MA, USA: Artech house, 2015.

[49] F. Xiao *et al.*, "Analysis of waveform retracking methods in Antarctic ice sheet based on CRYOSAT-2 data," *Int. Arch. Photogramm., Remote Sens. Spatial Inf. Sci.*, vol. 12, pp. 1561–1567, Sep. 2017.

[50] Y. B. Sulistioadi *et al.*, "Satellite radar altimetry for monitoring small rivers and lakes in Indonesia," *Hydrol. Earth Syst. Sci.*, vol. 19, no. 1, pp. 341–359, Jan. 2015.

[51] A. Egido and W. H. F. Smith, "Fully focused SAR altimetry: Theory and applications," *IEEE Trans. Geosci. Remote Sens.*, vol. 55, no. 1, pp. 392–406, Jan. 2017, doi: 10.1109/TGRS.2016.2607122.

[52] Y. Sheng, C. Song, J. Wang, E. A. Lyons, B. R. Knox, J. S. Cox, and F. Gao, "Representative lake water extent mapping at continental scales using multi-temporal Landsat-8 imagery," *Remote Sens. Environ.*, vol. 185, pp. 129–141, Oct. 2016, doi: 10.1016/j.rse.2015.12.041.
[53] H. Pella, E. Sauquet, and A. Chandesris, "Construction d'un réseau hydrographique simplifié à partir de la BD Carthage," in *Proc. Ingánieries Agricult.-Territoires*, 2006, pp. 3–14.
[54] S. Shu *et al.*, "Analysis of Sentinel-3 SAR altimetry waveform retracking algorithms for deriving temporally consistent water levels over ice-covered lakes," *Remote Sens. Environ.*, vol. 239, Mar. 2020, Art. no. 111643.
[55] S. W. Cooley, J. C. Ryan, and L. C. Smith, "Human alteration of global surface water storage variability," *Nature*, vol. 591, no. 7848, pp. 78–81, Mar. 2021.
[56] M. P. Maples *et al.*, "Robust chauvenet outlier rejection," *Astrophys. J. Suppl. Ser.*, vol. 238, no. 1, p. 2, Aug. 2018.

François Boy received the Engineering degree in physics from the École Centrale de Marseille, Marseille, France, in 2005, and the master's degree in electronics from the École nationale supérieure d'électrotechnique, d'électronique, d'informatique, d'hydraulique et des télécommunications, Toulouse, France, in 2006.

Then, he joined the Centre National d'Etudes Spatiales (CNES), Toulouse, where he is currently the technical coordinator of radar altimeter research and development activities over the ocean, inland waters, and ice surfaces.

Jean-François Crétaux is currently the Deputy Director and a member of the Scientist Council of the Laboratoire d'Etudes en Géophysique et Océanographie Spatiale (LEGOS), Toulouse, France, a Principal Investigator (PI) of the SWOT Mission, a member of the Terrestrial Observation Panel of Climate, a Scientist Leader of an ESA CCI project on lakes, and a Co-Lead of a NASA/CNES project on citizen for science. Over the last 20 years, he has contributed and led several international projects on space hydrology in different countries [Russia, Central Asia and Caucasus, Chili, India, and European Union (UE)]. He is the author or a coauthor of 76 articles in international journals.

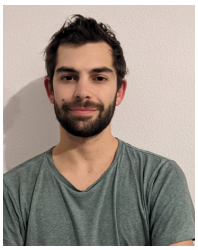

Malik Boussaroque graduated in physics and instrumentation from the l'Institut National des Sciences Appliquées de Toulouse (INSA Toulouse), Toulouse, France, in September 2020.

He is currently in charge of the activities related to spatial hydrology in the project context VOLODIA. This project aims at defining, validating, and promoting their scientific use and new methods of spatial data processing for hydrology. He joined Ocean-Next, La Terrasse, France, and the Laboratoire d'Etudes en Géophysique et Océanographie Spatiale (LEGOS), Toulouse, France, where he developed and maintained tools used in the VOLODIA project. He is also involved in the generation, update, and validation of the hydrological database of Sentinel-3&-6, Jason-3, and SWOT Missions that are used by space agencies to improve radar altimeter tracking (OLTC) on inland water.

Céline Tison received the Engineering and Ph.D. degrees from the École Nationale Supérieure des Télécommunications, Paris, France, in 2001 and 2004, respectively.

After conducting research and development studies on synthetic aperture radar (SAR) processing (polarimetry, high-resolution SAR, and interferometry), she was involved in the design and algorithm definition of the surface waves investigation and monitoring (SWIM) instrument scatterometer onboard the CFOSAT Mission. She is currently the Head of the Radar Instrument and Performance Department, Centre National d'Etudes Spatiales (CNES) (the French Space Agency), Toulouse, France.